ACS SENSORS

pubs.acs.org/acssensors
Article

A Novel Biosensor for Ferrous Iron Developed via CoBiSe: A Computational Method for Rapid Biosensor Design

Athanasios Papadopoulos, Manuel T. Anlauf, Jens Reiners, Seung-Hyun Paik, Aileen Krüger, Benita Lückel, Michael Bott, Thomas Drepper, Julia Frunzke, Holger Gohlke, Stefanie Weidtkamp-Peters, Sander H. J. Smits,* and Christoph G. W. Gertzen*

Cite This: *ACS Sens.* 2026, 11, 119−135

Read Online

ACCESS | Metrics & More | Article Recommendations | Supporting Information

ABSTRACT: Genetically encoded biosensors enable the monitoring of metabolite dynamics in living organisms. We present CoBiSe, a computational biosensor design approach using Constraint Network Analysis to identify optimal insertion sites for reporter modules in molecular recognition elements (MREs). Applied to the iron-binding protein DtxR from *Corynebacterium glutamicum*, CoBiSe identified a flexible connective loop (residues 138−150) for inserting the reporter module, resulting in IronSenseR, a novel ratiometric biosensor for ferrous iron (Fe^{2+}). IronSenseR demonstrates high specificity for Fe^{2+} with dissociation constants of 1.78 ± 0.03 ($FeSO_4$) and 2.90 ± 0.12 μM ($FeCl_2$), while showing no binding to Fe^{3+} and other divalent cations. *In vivo* assessment in *Escherichia coli*, *Pseudomonas putida*, and *Corynebacterium glutamicum* confirmed IronSenseR's capability to detect changes in the intracellular iron pool. The creation of IronSenseR underlines that by reducing search space and eliminating labor-intensive screening, CoBiSe streamlines biosensor development and enables precise creation of next-generation biosensors for diverse metabolites.

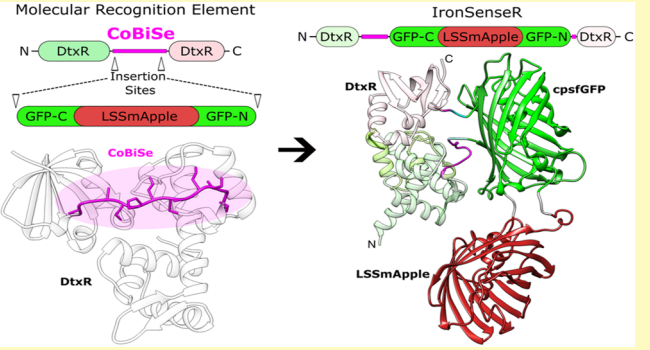

KEYWORDS: *computational biosensor design, IronSenseR, matryoshka, small-angle X-ray scattering (SAXS), specificity, bacteria*

Genetically encoded biosensors are minimally invasive tools that allow to monitor changes in various metabolite concentrations in living systems. Functional biosensors combine a molecular recognition element (MRE), which selectively binds a target metabolite, with a reporter module composed of one or more fluorescent proteins (FP). Fluctuations in metabolite concentration alter the binding to the MRE, which subsequently results in a modulation of the fluorescence signal of the reporter module that can then be detected.[1−3] This powerful feature enables monitoring of cellular dynamics and provides insights into complex metabolic processes with high spatial and temporal resolution.[4] The design of genetically encoded biosensors has traditionally relied on empirical approaches, where biosensors were created through trial-and-error processes.[1,4,5]

Typically, two biosensor designs are favored: The FRET-based biosensors rely on changes in FRET (Förster resonance energy transfer) between two FP domains, whereas the single-FP biosensors are based on environmental modulation of the fluorescence properties of the reporter FP.[1,6] In both biosensor designs, metabolite binding to the MRE induces conformational changes that lead to structural rearrangements of the entire biosensor protein, thereby modulating the fluorescence properties of the reporter module and enabling biosensing readout.[1,4,6,7]

FRET-based biosensors are relatively simple to design by sandwiching an MRE between a suitable donor and acceptor pair of FPs. In contrast, the creation of single-FP biosensors often requires a more sophisticated split of the MRE to insert the reporter module, which in turn allows to transmit the signal between both biosensor elements.[1,7] Commonly, single-FP biosensors utilize reporter modules that consist of at least a circular-permutated fluorophore (cpFP), which is fused into the MRE in a peculiar fashion.[7] This fusion of the reporter module to the MRE allows for an environmentally sensitive and conformational-dependent modulation of the fluorescence properties upon metabolite binding to the MRE.[7,8] Certainly, both popular biosensor designs, FRET-based and single-FP, present advantages and disadvantages: FRET-based biosensors

Received: July 10, 2025
Revised: November 21, 2025
Accepted: December 11, 2025
Published: January 11, 2026

are simple to design and can be used in a ratiometric fashion, but possess a comparably low signal-to-noise ratio, dynamic range, and sensitivity.[4,6] Single-FP biosensors overcome these limitations but support solely intensiometric measurement applications and are more challenging to create.[6,7]

The Matryoshka biosensor design was recently developed and combines the advantages of both previous biosensor designs.[9] It enables the creation of ratiometric biosensors that are excitable at a single wavelength and possess high signal-to-noise ratio, dynamic range, and sensitivity.[6,9,10]

While the empirical approach has yielded functional FRET-, single-FP, and Matryoshka biosensors in the past, it often requires the labor-intensive and time-consuming creation and screening of large libraries with putative biosensor variants.[5,11,12] Additionally, empirical biosensor design approaches may result in biosensors with limited specificity, sensitivity, or dynamic range, and such biosensors frequently require extensive downstream optimization to achieve adequate performance in a biological context.[5,12] In contrast, previous rational biosensor design approaches leverage detailed knowledge of molecular structures and binding mechanisms of the MRE to systematically engineer biosensors with predictable and tunable properties.[7] These processes are initiated by identifying or designing the biosensor's modular components, such as the individual MREs and FPs and their linking amino acid residues.[7] Computational modeling and structural biology allowed researchers to predict and enhance interactions between the MRE and its target metabolite, providing a more efficient way to achieve high specificity and affinity.[1] These predictions are often refined and validated experimentally by protein bioengineering approaches using site-directed mutagenesis and directed evolution to further optimize biosensor performance.[1,5] Although previous rational design approaches accelerated the development process and yielded biosensors that are inherently more robust, precise, and adaptable, the initial fusion of the MRE to the respective reporter module remained widely random.[1,3,5,7,13] Current rational approaches for biosensor creation, which already include structural analysis of the MRE, are mostly limited to probing loop regions or surface residues to identify suitable insertion sites.[14−18] This reduces the search space but is oblivious to the mechanical function of the MRE, thus maintaining too many putative insertion sites of the reporter module and still resulting in nonfunctional biosensor variants or affecting the biosensors' affinity and/or specificity. Therefore, a holistic structure-based approach to identify suitable insertion sites would be a major boost in biosensor development. Our goal was to develop a novel, fast, and robust method that allows the *in silico* prediction of insertion sites for the reporter module within the MRE without a loss of target metabolite binding properties. The resulting computational method for rapid biosensor design (CoBiSe) applies to MREs that are standalone binding proteins and in which metabolite binding induces conformational changes. Thus, the used MREs are complete binding proteins and not substructures or isolated domains of larger proteins and are not fusion constructs composed of multiple proteins or peptides. For the CoBiSe approach, several MREs were carefully analyzed, and only MREs that match the described requirements were considered to ensure the accuracy of the results.

The utilization of computational techniques in combination with structural analysis enabled the CoBiSe approach, which identifies flexible structure elements and distinguishes them from rigid clusters within the MRE. As a result, CoBiSe allows for the first time a highly reliable prediction of putative insertion sites for the fusion with the reporter module. The advantage of the CoBiSe approach is that it strongly reduces the large number of empirically identified or experimentally determined insertion sites. The fast identification of suitable insertion sites eliminates the pool of random insertions and clearly bypasses the previously required labor-intensive approaches. Thus, CoBiSe significantly reduces the overall duration and essentially enhances the biosensor creation process in comparison to previously utilized approaches.[5]

To verify that CoBiSe is suitable for the prediction of insertion sites, prominent pre-existing biosensors were used for retrospective insertion site analysis, and the results of identified insertion sites are in line with the described sites in the literature.[5,19−22]

Finally, CoBiSe was successfully utilized to create a completely novel biosensor for ferrous iron (Fe^{2+}). The global iron regulator DtxR[23,24] (Diphtheria toxin regulator protein) from *Corynebacterium glutamicum* served as MRE and was utilized for CoBiSe. DtxR senses Fe^{2+} within the bacterial cytosol and undergoes conformational changes that facilitate DNA binding, thereby enabling regulation of gene expression.[25,26] Accordingly, DtxR operates within a relevant Fe^{2+} -concentration range.[24] Structurally, DtxR is well characterized and presents two metal-binding sites.[27,28] Notably, the site formed by H79, E83, and H98 (metal-binding site I) coordinates a metal ion together with a cobound sulfate in deposited structures and bridges the N-terminal DNA-binding domain with the C-terminal SH3-like domain.[27] This results in a robust geometry-defined conformation that appears to be crucial for binding Fe^{2+} in the soluble $FeSO_4$ form. These features, including the compactly localized coordination chemistry, the putative domain-spanning allostery, the conformational stabilization upon iron binding, and the cytosolic expression and stability as well as the lack of disulfide dependencies meet greatly and directly onto CoBiSe's requirements for a well-posed MRE and predictable structural coupling. The physiological binding affinity and a deduced conformational change in the monomer rank it as a suitable candidate to test the CoBiSe pipeline to generate a novel ratiometric Matryoshka[9,10] biosensor that senses Fe^{2+}, a metabolite for which genetically encoded fluorescent-based biosensors barely exist.[29−34]

RESULTS AND DISCUSSION

A Retrospective Analysis Reveals the Robustness of the Rational Biosensor Design Approach by CoBiSe

First, we looked carefully at the insertion sites of the well-described single-fluorescent protein (FP) biosensors and tried to identify a rationale for the position of the fluorescent reporter module in the molecular recognition element (MRE). Here, the focus was on MRE into which reporter modules were inserted, which belong to the family of single-FP biosensors. The list of analyzed sensors comprises ATPqueen variant QUEEN7 μ,[20] RexYFP,[21] MalB2,[5] Tre-CO4,[5] HyPer3,[19] and PercevalHR.[22] Depending on the availability of their protein structures, either the experimentally determined structure or an AlphaFold model[35,36] of the MRE was used for further analysis. The respective structural information on the MREs was subjected to flexibility analysis by the Constraint Network

https://doi.org/10.1021/acssensors.5c02481
ACS Sens. 2026, 11, 119−135

Analysis (CNA) software using ensembles of network topologies and fuzzy noncovalent constraints (ENT^{FNC}), which does not require generating a structural ensemble but uses an ensemble of network topologies.[37,38] According to the results of the CNA analysis, regions of the MRE were selected as suitable insertion sites if they met three criteria: I. They are categorized as flexible at the start of or early in the thermal unfolding simulation by CNA. II. They are at the surface of the MRE, as adding the reporter module in the core would disturb the function greatly. III. They are close to the metabolite binding site or, preferably, they connect two different domains or secondary structure elements, that comprise the metabolite binding site. The latter was deemed more promising, as a larger movement is to be expected upon metabolite binding, which then may be transferred to the reporter module. These three steps comprise the workflow of CoBiSe that was implemented as a guided iterative pipeline that includes a series of computational and analytical steps (Figure 1). The closer the flexible sites are to the binding site and the earlier they become flexible during the thermal unfolding simulation, the more likely they were deemed to be insertion points. For the pre-existing biosensors, the CoBiSe approach resulted in predicted insertion sites in the MRE matching the reported insertion sites in the literature[5,19−22] (Figures 2 and S1). For QUEEN7 μ (Figure 2A), these are residues 106−111 as they are flexible residues that lie between the two helices connected by the binding site, with the reported insertion site being between residue 106−112, lacking the remaining residues. For RexYFP (Figure 2B), these are residues 79−81 as they are flexible residues that lay between two domains close to the binding site, with the reported insertion site between residues 79−80. The MRE of RexYFP can form a homodimer. Applying this method to the homodimer also predicts residues 78−81 as possible insertion sites (Figure S1). For MalB2 (Figure 2C), these are residues 193−195 and 204−208 as they are flexible residues that lay between the two domains connected via the binding site with the reported insertion site being between residues 195−196. For Tre-CO4 (Figure 2D), these are residues 95−101, 287−292, 335−337, and 362−366 as they are flexible residues that lay between the two domains connected via the binding site, with the reported insertion site being between residues 334 and 335. Here, due to the higher base rigidity of the MRE, these residues became flexible during step 7 of 136 of the thermal unfolding simulation. For HypPer3 (Figure 2E), the analysis predicted an insertion site located at positions 187−190 and 213−221 as they are flexible residues that are close to the site where a disulfide bridge is formed in the presence of hydrogen peroxide (H_2O_2), with the reported insertion site at residue 206. After the previous five successes, this prompted us to investigate further into the design of this biosensor. HyPer3 is an improved variant out of the HyPer series for which four possible insertion sites were identified in the MRE, of which the one at 206 showed the best ratiometric response, which is why it was chosen for further improvement.[39] The reported insertion sites in the MRE of HyPer and thus HyPer3 are between 205 and 206, 211 and 212, 214 and 215, and 218 and 219, with the latter two predicted via the CoBiSe approach. Finally, for PercevalHR (Figure 2F), the residues 26−41 and 54−59 are flexible residues that are close to the binding site, with the reported insertion site being between residues 53−54. Since PercevalHR can appear homotrimeric, the method was also applied to the trimer. Here, the range of residues is even smaller compared with the monomer with residues 37−41 and 54−55 (Figure S1). Thus far, our retrospective insertion site analysis predicted the same insertion sites for the reporter module as they were utilized for the described pre-existing biosensors (Figure 2). This poses the question of how much work the application of CoBiSe reduces in the biosensor creation process. Commonly, previous approaches screened for putative insertion sites throughout the whole MRE, and hence, this is a good starting point to estimate the efficiency of our approach. Considering the whole MREs respectively as possible insertion sites, using this approach means a reduction of the search space of 95% (6 vs 132) for QUEEN7 μ, 99% (3 vs 211) for RexYFP, 98% (8 vs 396 residues) for MalB2, 95% (21 vs 408) for Tre-CO4, 95% (13 vs 305) for HyPer3, and 80% (22 vs 112) for PercevalHR (Figure 2G,H). Hence, the application of our rational computer-based approach on average leads to an efficient reduction of the search space by 94% when screening for insertion sites within the whole MRE (Figure 2H). Some

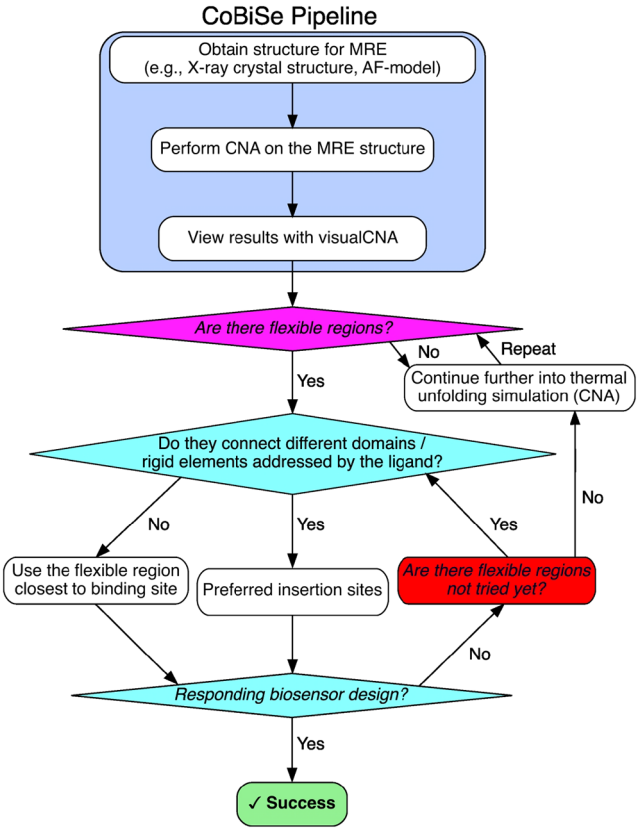

Figure 1. Schematic depiction of CoBiSe. The proposed scheme indicates crucial steps upon computational identification of putative insertion sites of biosensor cassettes into MREs that are key for the successful application of the Method. The CoBiSe decision workflow: Analyze MRE structures by CNA and inspect with visualCNA to identify flexible regions. When a flexible region exists, prioritize solvent-exposed loops that bridge rigid elements or domains as preferred insertion sites. If no bridging loop is available, select the flexible region closest to the binding site. Biosensor cassette insertions are built at the chosen loop(s) and screened for response signal upon ligand addition. Once responsive biosensor candidates are identified, the process completes (Success). If the straight path fails, test remaining flexible regions by repeating computational analysis. If still nonresponsive, switch the MRE or reporter. The process concludes upon identification of a reproducibly responding construct.

https://doi.org/10.1021/acssensors.5c02481
ACS Sens. 2026, 11, 119−135

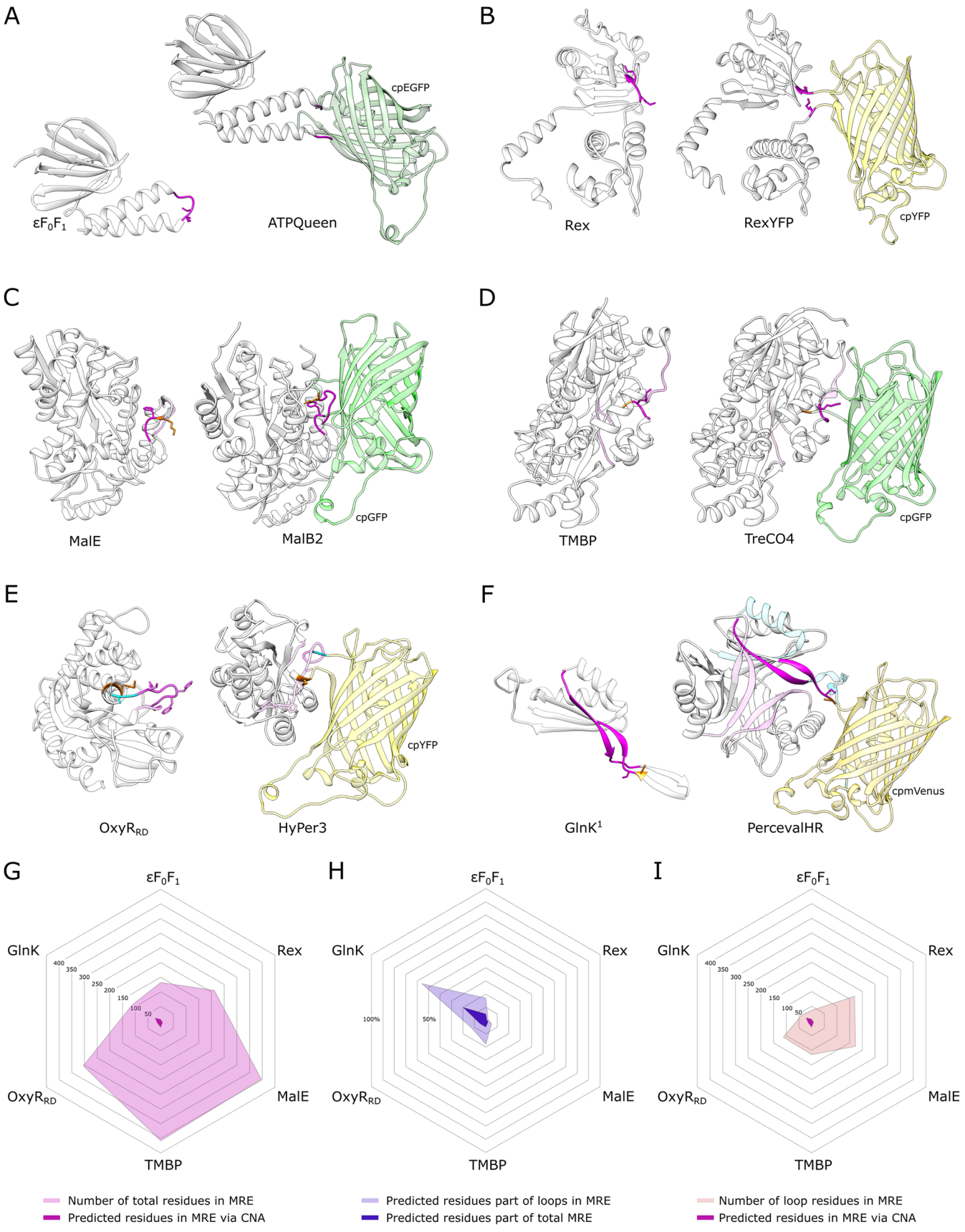

Figure 2. Computational determination of insertion sites for biosensor cassettes. The retrospective computational analysis indicates the utilized insertion sites for the circular-permutated fluorophores in preexisting biosensors. The AlphaFold3 (AF3) models of the substrate binding protein monomer (left) and the respective biosensor (right) are depicted. The computationally suggested insertion areas (magenta) are highlighted. Flanking residues (orange) and novel insertion sites (cyan) are indicated particularly. Utilized fluorophores are labeled and colored according to

https://doi.org/10.1021/acssensors.5c02481
ACS Sens. 2026, 11, 119−135

Figure 2. continued

their fluorescence emission. (A) The ε subunit of the bacterial F_0F_1 ATP-Synthase was utilized to create ATPQueen biosensor for ATP. (B) The bacterial transcriptional repressor Rex was utilized to create RexYFP biosensor for NAD^+/NADH ratio. (C) The bacterial maltose binding protein MalE was utilized to create MalB2 biosensor for maltose. The utilized insertion site is in line with the predicted area between the indicated flexible loop and the flanking amino acid residue. (D) The bacterial trehalose-maltose binding protein was utilized and modified to create Tre-CO4 biosensor for trehalose. The computational analysis determined multiple putative insertion areas (light rose), with the utilized site being most prominent. (E) The regulatory domain of OxyR H_2O_2 binding protein ($OxyR_{RD}$) utilized to create HyPer series of biosensors for H_2O_2. The predicted insertion sites are in line with the utilized areas for HyPer biosensor creation. Additional mutational screenings in terms of optimization of fluorescence parameters led to the novel insertion sites (orange and cyan) for HyPer3. (F) The nucleotide binding protein Gln *K* was utilized to create Perceval biosensor for ATP/ADP ratio. The protein is active as trimer and only one protomer is used for fluorophore insertion, whereby the determined insertion area is in line with the utilized site. The light cyan region in PercevalHR indicates structural elements of the protomer. (G) The total number of residues of all tested MREs is indicated (pink), and the predicted residues are highlighted (magenta). (H) The percentage of predicted residues compared to loop regions of the MREs (light blue) and the percentage of predicted residues compared to the total MREs are indicated (blue), showing the reduced amount of screening for putative insertion sites. (I) The number of residues in the loop regions of all tested MREs are indicated (rose) and the predicted residues are highlighted (magenta).

biosensor design approaches probe only in the loop regions of the MRE, as possible insertion sites can be identified there more frequently.[13] This reduces the search space, so that our approach must also compete against this rationale. If only the loop regions of the MRE are considered as a form of structure-based prediction, the reduction of the search space is 83% (6 vs 36) for QUEEN7 μ, 98% (3 vs 169) for RexYFP, 95% (8 vs 173 residues) for MalB2, 82% (21 vs 115) for Tre-CO4, 88% (13 vs 111) for HyPer3, and 44% (22 vs 39) for PercevalHR (Figure 2H,I). Of course, this metric is worse than before, but here CoBiSe still reduces the search space by 82% on average. When comparing the CoBiSe outcome to commonly used random site insertion or whole sequence screening, we achieve a reduction of up to 94% of the search space, whereas comparing it to a structure-aware approach, which only considers loop regions, CoBiSe achieves a reduction of the search space of on average 82% (Figure 2G–I). Detailed depiction for each pre-existing biosensor can be found in the Supporting Information (Figure S1). In summary, CoBiSe successfully identified insertion sites in six out of six MREs, and among those proteins identified seven out of nine insertion sites in a retrospective analysis in published biosensors (Figures 2 and S1). Furthermore, the applied computational analysis of insertion sites reduced the search space tremendously, regardless of whether the entire MRE or only the loop regions were analyzed.

To verify the robustness of CoBiSe in a prospective manner, we designed a completely novel ratiometric biosensor for ferrous iron (Fe^{2+}).

CoBiSe Analysis Enabled the Rapid Creation of a Biosensor for Ferrous Iron

By leveraging structural data in terms of finding a suitable iron binding protein for biosensor creation, the global iron regulator (Diphtheria toxin regulator protein, DtxR) from *Corynebacterium glutamicum* was identified. DtxR is a ferrous iron-binding protein that can serve as the molecular recognition element (MRE) for use in a putative ferrous iron (Fe^{2+}) biosensor. By applying the CoBiSe approach for DtxR, we identified putative insertion sites for the reporter module within the protein (Figure 3A). A flexible connective loop (residues 138–150) was identified as the optimal insertion site for the Matryoshka biosensor cassette, consisting of circularly permutated superfolder GFP (cpsfGFP) and large Stokes shift mApple (LSSmApple), which was successfully integrated into the DtxR protein. This amounts to a reduction in search space by 95% (13 of 230) for the complete MRE and 83% (13 of 74) considering only loop regions. Next, the Matryoshka biosensor cassette,[10] was successfully integrated in between every amino acid within the identified flexible connective loop of the DtxR protein (Figure 3A,B).

Putative iron biosensors were successfully expressed in *Escherichia coli*, with all designed variants exhibiting detectable expression levels as confirmed by downstream purification procedures (Figure S2). Subsequent purification of these variants was achieved by using affinity chromatography, yielding proteins that correspond to the expected molecular weight (MW) of approximately 80 kDa, as determined by SDS-PAGE (Figure S2). These results were in line with the expected theoretical MW of 84.19 kDa. The samples appeared pure in the SDS-PAGE (Figure S2A), and the in-gel fluorescence revealed no other bands, suggesting that no major fluorescent degradation products occurred, and more importantly, no interfering fluorescence signal will arise during further fluorimetric analysis upon titration of metal ions (Figure S2B). Next, the putative biosensor variants were screened for iron-sensing action (Figure 3C). Functional characterization of the purified biosensors was conducted by fluorimetric analysis screening for their response to iron (II) sulfate ($FeSO_4$) titrations (Figure 3C). Insertion variants at positions I138, D141, D147, S148, and G149 displayed an obvious ferrous iron (Fe^{2+}) concentration-dependent increase in cpsfGFP fluorescence compared to their unbound state (Figure 3C). This indicates a robust and positively responsive configuration for these sites, suggesting enhanced sensitivity to structural changes of DtxR induced by ion binding. Conversely, insertion variants at position G139, L140, Q142, A143, D144, P146, and V150 exhibited only moderate changes in fluorescence intensity, suggesting a more subdued responsiveness in these configurations (Figure 3C). Out of all tested variants, E145 indicated a negative response correlation of cpsfGFP fluorescence upon ferrous iron binding (Figure 3C). In summary, the functional characterization revealed five insertion variants (I138, D141, D147, S148, and G149) displaying robust positive responses to ferrous iron (0–25 μM) with dynamic ranges exceeding 50% (Figures 3 and S2). These variants exhibited significant concentration-dependent increases in cpsfGFP fluorescence upon binding of ferrous iron (Fe^{2+}), with dynamic ranges between 84.4% and 107%, demonstrating their enhanced sensitivity to DtxR structural changes induced by iron binding (Figure 3C). The dynamic range was employed to facilitate quantitative comparisons among the different biosensor variants by providing a normalized metric (Figure 3D). Twelve variants indicated an

https://doi.org/10.1021/acssensors.5c02481
ACS Sens. 2026, 11, 119–135

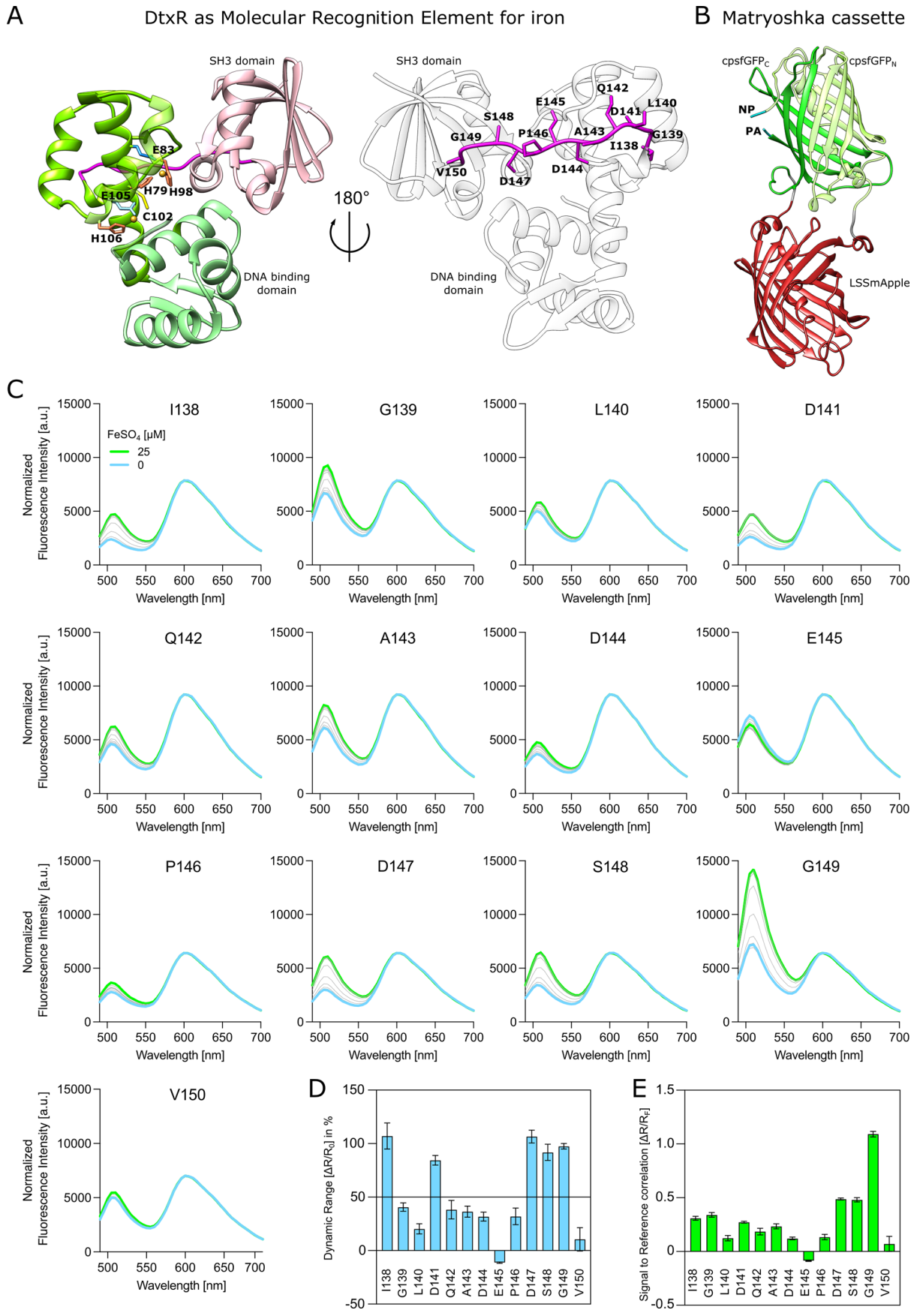

Figure 3. Identification of suitable insertion sites for the creation of responsive biosensors for iron ions. (A) The AlphaFold3 (AF3) model of DtxR from *C. glutamicum* is depicted. The protein serves as molecular recognition element for iron. The metal-binding sites of DtxR (MBS1: H79, E83, H98 and MBS2: E105, C102, H106) and coordinated metal ions are shown. Subdomains (SH3 domain and DNA-binding domain) are indicated.

https://doi.org/10.1021/acssensors.5c02481
ACS Sens. 2026, 11, 119−135

Figure 3. continued

The flexible loop (magenta) indicates residues that are used as putative insertion sites for the Matryoshka cassette. (B) The AlphaFold3 model of the Matryoshka cassette is depicted, the cassette consists of a nested LSSmApple (red) nested to a circular-permutated superfolder GFP (cpsfGFP, green). Due to the permutation the amino and carboxy termini of sfGFP sequence are switched, thus the original C-terminal sequence (sfGFPc, green) appears before the original N-terminal sequence ($sfGFP_N$, light green). The linker residues (PA and NP) are indicated. (C) The titration of $FeSO_4$ (0−25 μM) used to monitor the sensing action of DtxR-based ratiometric biosensor variants when insertion of the matryoshka cassette conducted at the proposed positions within the identified flexible loop. (D) The dynamic range of the respective biosensor variants is depicted [$\Delta R/R_0$, %]. (E) The signal-to-reference correlation of the cpsfGFP intensities to the intensity of the reference fluorophore is depicted. The response was monitored as an increase of cpsfGFP fluorescence upon ion binding. The variant created upon insertion at position G149 indicates enhanced dynamic range and signal-to-noise ratio in comparison to the other biosensor variants. For the data on the sensing action of putative biosensor, at least two technical replicates (n = 2) are depicted, mean values (in C, D, and E) and the standard deviation (SD) (in D and E) are indicated.

increase in the dynamic range, underlining a positive sensing mode of the novel Matryoshka iron biosensors. Here, five variants indicated an enhanced dynamic range above 50%, being I138 with 107%, D141 with 84.4%, D147 with 106.6%, S148 with 91.8%, and G149 with 97.5% (Figure 3D). Next, to assess the dynamic behavior among the five most responsive variants, the signal-to-reference correlation of the biosensors was evaluated to determine which variant yields the best signal-to-noise ratio (Figure 3E). Among the tested biosensor variants, the one created by insertion of the reporter module at position G149 of DtxR demonstrated the highest signal-to-reference correlation, indicating superior signal-to-noise ratio, sensitivity, and responsiveness to ferrous iron (Figure 3E). These results highlight that the insertion at position G149 created the most effective iron biosensor $MDtxR_{G149}GA$. The superior biosensor variant $MDtxR_{G149}GA$ was named IronSenseR.

Characterization of IronSenseR

The IronSenseR was characterized *in vitro* by biochemical and structural analysis (Figure 4). Structural investigations by small-angle X-ray scattering (SAXS) confirmed the monomeric state of the biosensor in solution; furthermore, we compared the theoretical scattering intensity of the AF3 predicted models and identified the best-fit model ($\chi 2$ = 1.08) with the experimental data (Figures 4A and S6, Table S1). IronSenseR indicates an enhanced dynamic range for ferrous iron (Fe^{2+}) in the form of iron (II) sulfate ($FeSO_4$) (Figure 4B). To assess the specificity of the biosensor toward further ions, ferrous iron in form of iron (II) chloride ($FeCl_2$), ferric iron (Fe^{3+}) as iron (III) sulfate ($Fe_2(SO_4)_3$) and iron (III) chloride ($FeCl_3$), manganese (II) sulfate ($MnSO_4$), cobalt (II) sulfate ($CoSO_4$), cupper (II) sulfate ($CuSO_4$), zinc (II) sulfate ($ZnSO_4$), nickel (II) sulfate ($NiSO_4$), magnesium (II) sulfate ($MgSO_4$) and calcium sulfate ($CaSO_4$) as well as calcium chloride ($CaCl_2$) were used for further investigations (Figures 4C and S3). Fluorimetric binding analysis upon ion titrations revealed the highest affinity for Fe^{2+} in the form of $FeSO_4$, with a dissociation constant (K_d) of 1.78 ± 0.03 μM, indicating strong and specific binding (Figure 4C). Similarly, the biosensor showed high affinity for $FeCl_2$, with a K_d of 2.90 ± 0.12 μM, being within a comparable range to that of $FeSO_4$ (Figure 4C). In contrast, negligible changes in cpsfGFP fluorescence and dynamic range were observed for $Fe_2(SO_4)_3$, $FeCl_3$, $ZnSO_4$, $NiSO_4$, $MgSO_4$, $CaSO_4$, and $CaCl_2$, suggesting minimal to no binding to these compounds (Figures 4C and S3A−K). A slight response was detected for $MnSO_4$, but exhibited a significantly reduced dynamic range compared to those of $FeSO_4$ and $FeCl_2$ (Figure 4C). Interestingly, $CoSO_4$ and $CuSO_4$ displayed titratable binding but did not reach saturation in the applied concentration range, implying a lower affinity (Figure 4C). These findings demonstrate that IronSenseR preferentially binds ferrous iron (Fe^{2+}), while showing little to no interaction with ferric iron (Fe^{3+}) or other tested metal ions (Figure 4C). To address whether the obtained data are indeed due to the binding of ferrous iron to the biosensor, binding-deficient mutants were created and utilized for fluorimetric analysis upon titration of $FeSO_4$. As described in the literature, DtxR contains two metal ion binding sites (MBS 1 and 2).[27] To create binding-deficient biosensors, the coordinating residues H79, H98, and C102 were exchanged with alanine.[27,28] The corresponding mutants of MBS1, H79A and H98A, indicate nearly no binding to ferrous iron (Figures 4D and S3L−N). Negligible changes in fluorescence were observed for MBS 2 mutant C102A, concluding also no binding to ferrous iron in a relevant concentration range (Figures 4D and S3N). Taken together, the described results demonstrate the capability of IronSenseR to selectively bind ferrous iron. Moreover, the results point to the specificity and suitability of the biosensor for detecting ferrous iron over ferric iron or other divalent cations under *in vitro* conditions.

Assessment of Genetically Encoded Biosensor for Ferrous Iron *In Vivo*

After *in vitro* characterization, IronSenseR was assessed *in vivo* in *Escherichia coli* via fluorescence microscopy. Bacteria were cultivated in nutrient-rich media, and iron availability was subsequently altered after cell growth by adding varying concentrations of the membrane-permeable iron chelator 2,2′-bipyridine (BPD).[40,41] This was done since iron plays an essential role in the growth and viability of cells, so that alteration of iron homeostasis is challenging and often affects cell growth and protein expression.[42] Microscopy data revealed a reduction in the fluorescence ratio of cpsfGFP/LSSmApple upon increasing BPD concentration (from 1.0 without chelator to 0.84 with 250 μM BPD), with cpsfGFP fluorescence decreasing, while LSSmApple fluorescence remained constant (Figures 5 and S4A−E). Additionally, binding-deficient mutants H79A, H98A, and C102A of IronSenseR did not indicate ratiometric changes upon addition of BPD or were greatly diminished in comparison to the wild-type IronSenseR (Figures 5 and S4A−E). The ratiometric design allowed analysis of cells with heterogeneous expression levels. While the apparent dynamic range *in vivo* was reduced compared to *in vitro* measurements, likely due to the indirect alteration of intracellular iron and challenges in accurately detecting the change of intracellular iron concentrations, the decreasing cpsfGFP/LSSmApple ratio is in line with the expected sensing mode of IronSenseR. In summary, these results demonstrate

https://doi.org/10.1021/acssensors.5c02481
ACS Sens. 2026, 11, 119−135

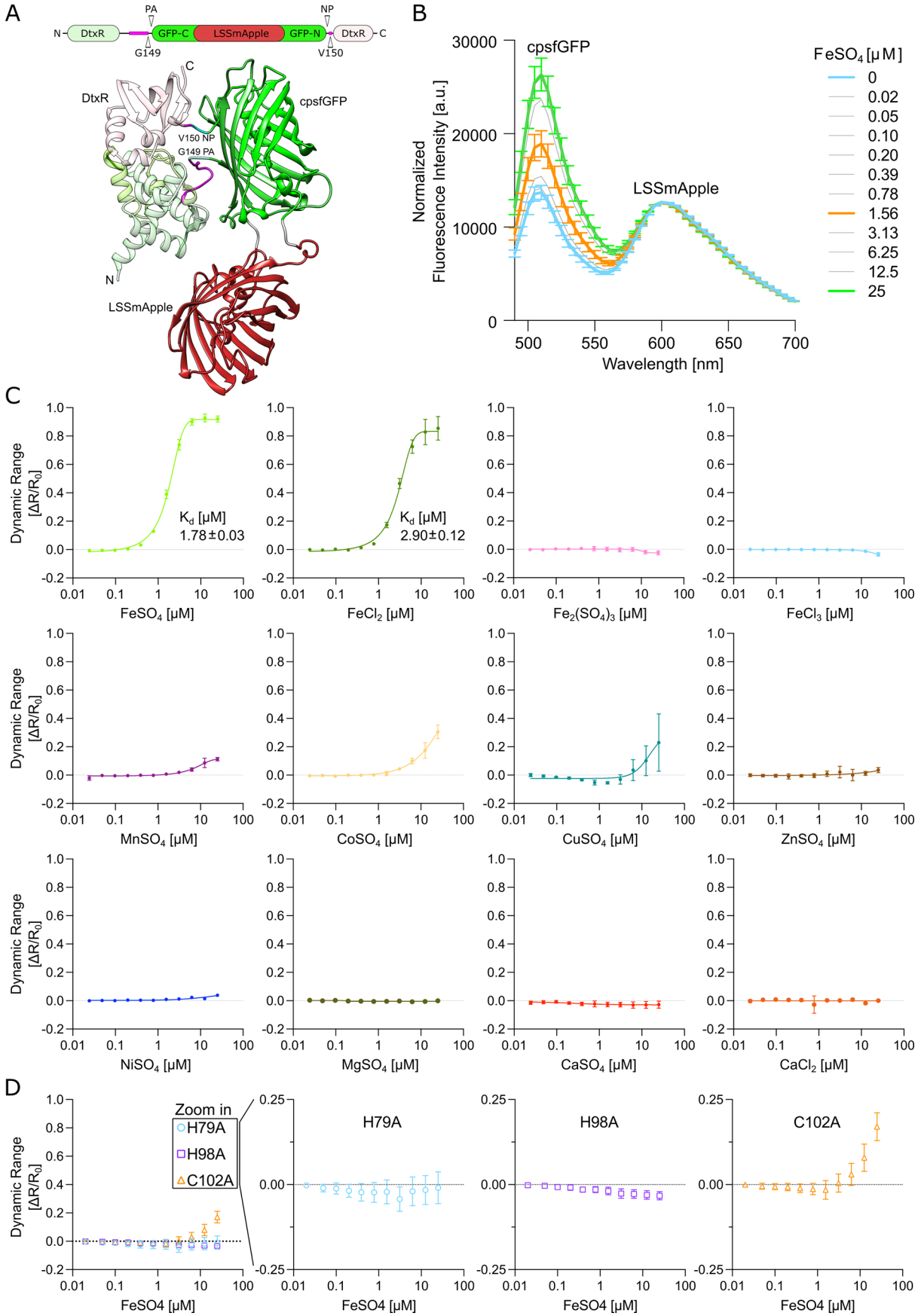

Figure 4. Characterization of IronSenseR: A ratiometric biosensor for ferrous iron. (A) Molecular architecture and AlphaFold3 (AF3) model of IronSenseR, the Matryoshka biosensor for iron is depicted. The flexible loop (magenta) and the insertion site G149 for the Matryoshka cassette are indicated. (B) The titration of $FeSO_4$ (0−25 μM) used to monitor the function of the ratiometric biosensor. (C) The change of the fluorescence

https://doi.org/10.1021/acssensors.5c02481
ACS Sens. 2026, 11, 119−135

Figure 4. continued

intensities of the reporter FP (cpsfGFP) used to calculate the dynamic range [$\Delta R/R0$] of IronSenseR upon titration of various metal ions at different concentrations. The binding affinities (K_d's) are indicated as mean values with standard error of the mean (SEM). (D) The dynamic range for binding-deficient IronSenseR mutants H79A, H98A, and C102A. The zoom-in serves for a more detailed view on the data. All the data shown are averages of at least three biological replicates (n = 3); mean values and the standard deviation (SD) are indicated.

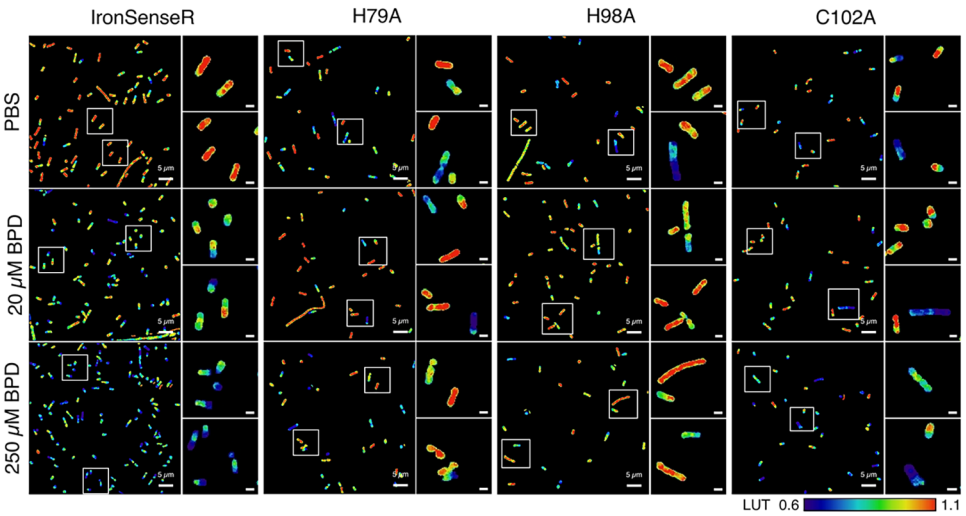

Figure 5. *In vivo* imaging of IronSenseR in *Escherichia coli* Response of IronSenseR and binding-deficient mutants (H79A, H98A, and C102A) to increasing concentrations of the iron chelator 2,2′-bipyridine (BPD) in bacterial cells. Confocal images of *E. coli* BL21(DE3) expressing the biosensor without addition of BPD (0 μM, PBS top row) and after incubation with either 20 μM BPD (middle row) or 250 μM BPD (bottom row) are depicted. The ratio of green (cpsfGFP) to red fluorescence (LSSmApple) is displayed using a rainbow-colored lookup table with two zoomed-in sections depicted next to the main columns. The scale bar in the zoomed-in images is 1 μm. LUT 0.6−1.1 is depicted by the color bar (down right), indicating the decrease in ratio G/A upon BPD addition. When iron is present, the ratio G/A and LUT is high (red) but drops (blue) when iron is chelated by BPD for IronSenseR WT. In case of the binding-deficient mutants, this effect is not observable for H79A and H98A or highly diminished as for C102A. Data acquired in biological replicates, n = 6 for WT and n = 3 for binding-deficient mutants.

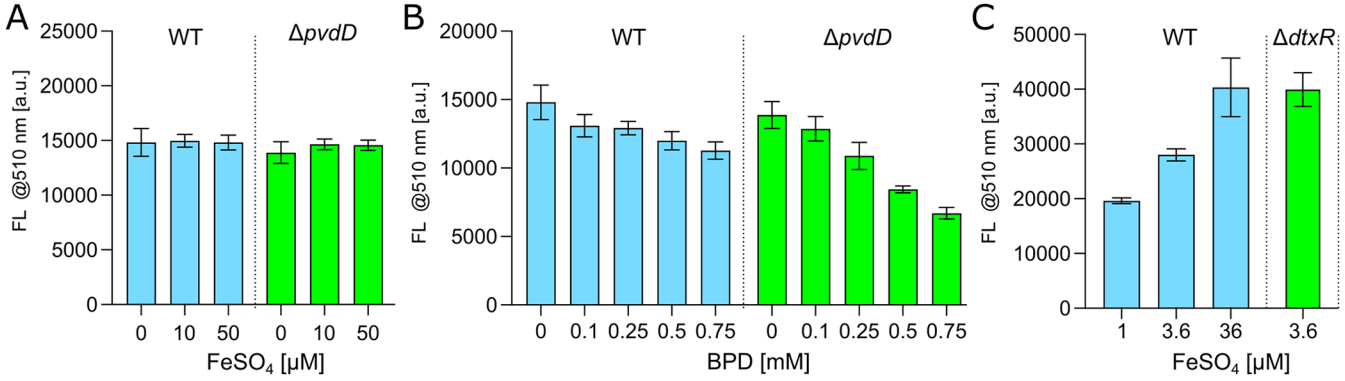

Figure 6. *In vivo* iron sensing in *Pseudomonas putida* and *Corynebacterium glutamicum*. Response of IronSenseR to increasing concentrations of the iron chelator 2,2′-bipyridine (BPD) and ferrous iron ($FeSO_4$) was determined via fluorescence analysis in the *P. putida* wild type (WT) and pyoverdine-lacking mutant (Δ*pvdD*) strain. (A) Comparison of reporter fluorescence (FL) at 510 nm between *P. putida* WT and Δ*pvdD* upon addition of ferrous iron ($FeSO_4$). (B) Comparison of reporter fluorescence (FL) at 510 nm between *P. putida* WT and Δ*pvdD* upon addition of BPD. (C) IronSenseR utilized to sense varying iron content upon cultivation of *C. glutamicum*. Increasing iron uptake and/or availability led to increasing reporter fluorescence of IronSenseR. Comparison of *C. glutamicum* WT and Δ*dtxR* strains upon cultivation in 3.6 μM iron and expression of IronSenseR. The mutant strain Δ*dtxR* lacks the regulation of iron acquisition and is not limited in comparison to the WT; therefore, IronSenseR signal is increased, indicating a large pool of intracellular iron in comparison to the WT. The experiments were conducted in biological replicates, six for *P. putida* (n = 6) and four for *C. glutamicum* (n = 4). The mean values and the standard deviation (SD) are indicated.

that the ratiometric IronSenseR can effectively measure dynamic changes in intracellular iron levels in *E. coli*.

Next, the IronSenseR was utilized in *Pseudomonas putida* and *Corynebacterium glutamicum*, to demonstrate the broad applicability of the biosensor in different bacteria (Figures 6 and S5). The corresponding IronSenseR encoding gene cassette was codon-optimized for its use in *P. putida*, a Gram-negative bacterium relevant to biotechnology and siderophore-based microbial interactions.[43,44] Under iron-depleted conditions, various *Pseudomonas* species produce and secrete the siderophore pyoverdine, which binds environmental ferric iron. The ferri-pyoverdine complex can be specifically taken up by the bacteria, thereby playing an important role in bacterial iron homeostasis.[45] To test if

https://doi.org/10.1021/acssensors.5c02481
ACS Sens. 2026, 11, 119−135

changes in the cytosolic iron pool in *P. putida* can be detected by IronSenseR, the biosensor encoding gene cassette was genomically integrated into wild-type strain KT2440 and a pyoverdine-deficient mutant strain (Δ*pvdD*). The recombinant biosensor strains were grown under iron-supplemented and iron-depleted conditions. As indicated by the constant fluorescence ratios of the biosensor, increasing the iron concentration in the growth medium did not affect the labile iron pool in the cells of either strain (Figures 6A,C and S5A,B). However, due to the loss of siderophore-mediated iron acquisition in the Δ*pvdD* strain, increasing concentrations of BPD led to a detectable decrease in the cytosolic pool of free ferrous iron and a reduction in the fluorescence intensity of the biosensor reporter domain. Conversely, the gradual depletion of iron resulted in the induction of pyoverdine biosynthesis in the wild-type strain, thereby maintaining the intracellular iron pool at a constant level (Figures 6D,F and S5C,D). These observations confirm the important role of pyoverdine in iron homeostasis and thereby clearly prove the *in vivo* applicability of IronSenseR.

C. glutamicum expressing IronSenseR was cultivated with varying iron concentrations from a standard high amount of 36 μM, over a sufficient one of 3.6 μM to a limitation of 1 μM (Figures 6G and S5E). A clear reduction in reporter (cpsfGFP) fluorescence emission signal can be observed with decreasing iron concentrations. Moreover, a deletion mutant strain (*C. glutamicum,* Δ*dtxR*) was transformed with the IronSenseR encoding plasmid and iron-dependent reporter signals compared to the wild type. DtxR is the master regulator of iron homeostasis in *C. glutamicum*, acting as an iron-activated repressor of iron starvation response.[23] A mutant lacking *dtxR* was previously shown to show enhanced expression of several operons encoding iron uptake systems. Therefore, it was expected that the mutant accumulates and maintains high intracellular iron levels in comparison to the wild type, due to further iron uptake despite iron sufficiency. Using IronSenseR, the expected effect could be observed under the 3.6 μM iron condition, indicated by an increased reporter emission signal in comparison to the wild type (Figures 6H and S5F). Additionally, it is crucial to note that the Δ*dtxR* mutant possesses a growth defect due to iron overload.[24] This growth defect was indeed observed upon monitoring the optical density (OD600) upon cultivation, indicating that DtxR-based IronSenseR does not complement the deletion phenotype in *C. glutamicum*.

CONCLUSIONS

The development of biosensors has advanced significantly, transitioning from traditional empirical design approaches to rational, computationally informed strategies.[1,5,7,13] Empirical design, while foundational, relies heavily on trial-and-error approaches that are time-consuming, inefficient, and often yield suboptimal biosensors requiring extensive refinement.[1,46] In contrast, rational design leverages molecular knowledge and computational tools to systematically engineer biosensors with predictable and tunable properties.[1,7,13] The power of the computational biosensor design (CoBiSe) approach is based on Constraint Network Analysis (CNA).[37,38] In combination with structural analysis, CNA facilitates the identification of flexible structural elements within molecular recognition elements (MREs) and allows the reliable prediction of optimal insertion sites for reporter modules (Figure 1). We demonstrated that our computational approach, CoBiSe, retrospectively predicted insertion sites over a diverse set of MREs, which had been utilized in pre-existing prominent biosensors and are not substructures of larger binding proteins or fusion proteins (Figure 2). Moreover, CoBiSe prospectively enabled the successful design of a novel ratiometric Matryoshka biosensor for ferrous iron named IronSenseR.

For the retrospective computational analysis of insertion sites in pre-existing biosensors, we used either high-quality X-ray crystal structures or AlphaFold models of the MREs.[35,36] For multimeric MREs, both the multimeric structure and single protomers were analyzed, with both approaches correctly predicting the insertion sites (Figure 2A–F). This demonstrates the robustness of our approach, showing that no specific structural state or method of structure determination is required. Knowledge of active and inactive protein states is also not a prerequisite, although we are investigating methods to exploit such information to further reduce the search space (Figure 2G–I). Additionally, the ENT^{FNC} approach implemented in CNA enables this method even when resources for computationally intensive tasks like molecular dynamics simulations are unavailable.[38] Furthermore, MREs with similar folds shared predicted flexible regions (e.g., both MalE in MalB2 and TMBP in Tre-CO4 exhibit a Venus fly trap mechanism) (Figures 2 and S1), supporting our fundamental concept of viewing MREs as mechanical structures with rigid and flexible parts that move in specific ways to function. This idea is corroborated by investigations showing strong correlations between protein structure and dynamics.[47] Ideally, function should remain undisturbed, so we aim to insert reporter modules in flexible parts less likely to participate in the MRE's concerted mechanical movements. Insertion sites are not exclusively found in loop regions (though there is a preference), making the CNA flexibility prediction advantageous. Both predicted and experimentally identified sites predominantly occur at transitions between flexible and rigid regions (Figures 2 and S1), supporting our hypothesis that when rigid parts move in concert, the maximum force is exerted at these transitions.

To validate the capability of CoBiSe to predict suitable insertion sites for *de novo* biosensor creation, we applied our approach to the global iron regulator protein DtxR from *Corynebacterium glutamicum* with the aim to create a ratiometric biosensor for ferrous iron (Fe^{2+}) (Figure 3A). Ferrous iron plays central roles in numerous cellular processes, serving as a cofactor in oxygen transport, redox reactions, energy production, and gene regulation for bacteria as well as in general for living cells.[42,48,49] Its chemical reactivity promotes the generation of damaging reactive oxygen species (ROS),[50] necessitating tight cellular regulation to balance essential functions against potential toxicity.[50] Previous attempts to create biosensors for ferrous iron resulted in limited or indirect detection methods.[29−33] CoBiSe predicted insertion sites that led to the successful creation of multiple active biosensor candidates for ferrous iron and allowed the immediate identification of a superior biosensor variant (Figure 3). Our CoBiSe approach identified a flexible connective loop between I138 and V150 of DtxR as putative insertion sites for the reporter module (Figure 3A). Inserting the next-generation Matryoshka cassette[10] (Figure 3B) into these positions yielded 13 ratiometric biosensor candidates that were rapidly screened for ferrous iron binding in vitro (Figure 3C). The variant with insertion at position G149 demonstrated superior sensing behavior and high specificity for

https://doi.org/10.1021/acssensors.5c02481
ACS Sens. 2026, 11, 119−135

Fe^{2+} in the physiological micromolar range, without binding to other relevant cations such as Fe^{3+} (Figures 3C and 4). The next-generation Matryoshka biosensor module provided enhanced signal-to-noise ratio, allowing finely tuned responses upon iron binding (Figure 3C−E). The novel ratiometric IronSenseR indicated a high affinity toward ferrous iron *in vitro*, with dissociation constants in the single-digit micromolar range (K_d's are 1.78 ± 0.03 μM for $FeSO_4$ and 2.90 ± 0.12 μM for $FeCl_2$) (Figure 4).

Next, IronSenseR was successfully applied for *in vivo* analysis of the intracellular iron pool in different bacterial cells (Figures 5 and 6), addressing a critical need for precise and selective detection of ferrous iron in biological contexts.[29,30] The precise correlation between fluorescence ratios and exact or absolute concentrations of Fe^{2+} in the cells remains challenging. This limitation is not unique to IronSenseR but applies broadly to all biosensors and metabolites measurements.[51] Biosensors serve as valuable tools for estimating intracellular metabolite concentration ranges, which can be refined by biosensor variants with different affinities.[20,52] Additionally, the response of biosensors to metabolite concentrations can vary greatly depending on the microenvironment.[51,53] Factors such as pH, temperature, ionic strength, and molecular crowding can all influence the sensitivity and apparent dynamic range of the biosensor.[51] IronSenseR indicates optimized dynamic range, specificity, and sensitivity, demonstrating the adaptability of our design framework. The successful and rapid creation of IronSenseR validates that the CoBiSe approach eliminates the need for labor-intensive empirical biosensor creation[1,5] and accelerates the creation process while ensuring optimal biosensor performance in a single step.

IronSenseR represents a significant advancement with potential applications in studying iron homeostasis and its dysregulation in cells. Beyond basic research, a tool like IronSenseR can support screenings of iron-related functions in bacterial pathogens.[49] Moreover, by providing a precise and reliable method to explore iron-dependent biochemical pathways and cellular processes, IronSenseR supports various research areas.

CoBiSe transforms rational biosensor design by strategically combining structural and computational information, making it adaptable to virtually any standalone binding protein of interest. The CoBiSe approach enables rapid biosensor creation regardless of the target metabolite, as demonstrated by IronSenseR. By significantly narrowing the search space for the insertion of the reporter module, CoBiSe offers an efficient, rational, and more economically and environmentally sustainable biosensor design approach. Its broadly compatible computational requirements ensure accessibility to the aforementioned resources across the scientific community.

EXPERIMENTAL SECTION

Computational Insertion Site Identification

CoBiSe was implemented as a guided iterative pipeline that includes a series of computational and analytical steps. CoBiSe pipeline was utilized to identify putative insertion sites (Figure 1). The molecular recognition elements (MREs) of interest were analyzed by Constraint Network Analysis (CNA).[37,38,54] Flexible regions identified by CoBiSe in MREs were prioritized as solvent-exposed loops between rigid domains and selected as the preferred insertion sites. If no such bridging loop was available, the flexible region closest to the ligand-binding site was selected. For the application of the CNA[37,38,54] approach in the retrospective analysis on the MREs of the single-fluorescent protein (FP) biosensors, X-ray crystal structures or AlphaFold models[35,36] or available models from the UniProtKB[55] were used. Here, a deliberate mix of experimentally determined crystal structures and AlphaFold models was used, although an emphasis was put on crystal structures with high sequence coverage and low resolution. Only those MREs were selected that are standalone binding proteins and not substructures of larger binding proteins or represent a fusion of two proteins and/or peptides.

For HyPer3,[19] PercevalHR,[22] and MalB2,[5] AlphaFold[35,36] models were used, and for RexYFP,[21] ATPQueen variant QUEEN7 μ,[20] and Tre-CO4,[5] the PDB entries 2DT5,[56] 2E5Y,[57] and 1EU8[58] were used, respectively. The structures were prepared using the protein preparation wizard in Maestro and protonated to a pH of 7.4 using PROPKA.[59] Subsequently, the structures were analyzed using the CNA approach.[54,60] For analyzing the rigid cluster decomposition of all MREs, a constraint dilution simulation was performed using CNA on an ensemble of network topologies generated via fuzzy noncovalent constraints (ENT^{FNC}).[37,38] Subsequently, the unfolding trajectory was visually inspected using VisualCNA[54] for regions that were determined to be flexible, preferably at the beginning of the thermal unfolding simulation, and that are either near to the metabolite binding site or, preferably, that connect rigid domains that are addressed by the metabolite. VisualCNA is an easy-to-use PyMOL[61] plugin that allows setting up CNA runs and analyzing CNA results, linking data plots with molecular graphic representations.[54] For the generation of the novel IronSenseR, an AlphaFold model of the DtxR iron-binding protein originating from the *Corynebacterium glutamicum* strain (Uniprot ID: Q8NP95) was treated as described above and utilized as MRE for subsequent investigations. Here, design decisions followed the CoBiSe pipeline (Figure 1). Constructs were then built at the chosen putative insertion sites and tested for the response. Created biosensor variants were screened for binding ferrous iron, as described below. The iterative character of the CoBiSe pipeline allowed us to discriminate not only putative insertion sites for functional biosensor creation but also enables the discrimination of superior biosensor variants within the pool of created candidates. Alternatively, if no responding biosensor variant is obtained, the remaining flexible regions can be further analyzed and utilized for insertion of the biosensor cassette. Once a responding design is identified, the procedure is concluded. If no untested flexible regions are evident, then the thermal unfolding simulation can be viewed at higher temperatures to reveal further putative insertion sites. If no such bridging loop between ligand-binding domains is available, then the selected flexible region closest to the ligand-binding site can be tried out.

Molecular Cloning

The *dtxR* gene was amplified by PCR from gDNA of *Corynebacterium glutamicum* strain ATCC13032 and subcloned into $pRSET_B$-based vector, and subsequently, the correctness was verified by sequencing (Microsynth Seqlab). This vector was linearized by PCR to be used for the Gibson assembly. The Matryoshka cassette,[10] encoding for the circular-permutated superfolder GFP[62] (cpsfGFP) and nested large Stokes shift mApple (LSSmApple),[10] was amplified by PCR with corresponding primers possessing suitable ends for Gibson assembly and inserted into the respective insertion sites of DtxR (I138−V150). After PCR, samples were treated with DpnI (NEB) and analyzed by agarose gel electrophoresis. The corresponding amplicons were isolated by gel extraction (Macherey-Nagel, gel clean-up kit) and utilized for Gibson assembly (NEB). Binding-deficient mutants of the biosensor were created by site-directed mutagenesis using the KLD mix (NEB). The cloning constructs were used to transform chemically competent *Escherichia coli* DH5α (NEB) by the heat shock method. Positive clones were obtained upon cultivation of LB (lysogeny broth, Luria/Miller, Roth) agar plates containing 100 μg/mL ampicillin. Single colonies were used for cultivation in LB supplied with the same antibiotics and were utilized for plasmid isolation (Macherey-Nagel, Plasmid isolation kit). The plasmids were subjected to DNA sequencing (Microsynth) to confirm successful cloning. Primers for DNA amplification were used with corresponding

https://doi.org/10.1021/acssensors.5c02481
ACS Sens. 2026, 11, 119−135

primers listed in the Supporting Information (Table S2). All kits and protocols followed the manufacturer's guidelines.

To apply IronSenseR *in vivo* in *Pseudomonas putida*, the corresponding encoding gene cassette of IronSenseR was optimized using the galaxy codon harmonizer.[63] The resulting biosensor gene was cloned via Gibson assembly[64] into a miniTn7 vector under the control of a P_{tac} promoter regulated by the *lac* repressor LacI.[65] To analyze if the loss of siderophore production results in a detectable change of the intracellular pool of free iron ions, the pyoverdine biosynthesis gene *pvdD* was deleted using the pQure system.[66] Using triparental conjugation, the biosensor expression cassette located on plasmid (pAZ191_GA) was transferred to *P. putida* and subsequently integrated into the genome (Tn7 insertion site) of both the *P. putida* WT strain KT2440 and the Δ*pvdD*, as described previously.[67]

For the *in vivo* usage of IronSenseR in *Corynebacterium glutamicum*, the plasmid vector was exchanged to the shuttle vector pPREx2,[68] including an IPTG-inducible *tac*-promoter and a kanamycin resistance cassette, while protein tags were removed. Molecular methods were performed according to standard protocols.[69] Plasmids were enzymatically assembled using Gibson Assembly,[64] resulting in pPREx2-MDtxR$_{G149}$GA amplified and stored in *E. coli* DH5α.

Expression and Purification

Biosensor encoding gene cassettes were expressed in *Escherichia coli* BL21 (DE3), and the corresponding proteins were purified by affinity chromatography. In brief, each biosensor variant was encoded by a pRSET$_B$-based expression system containing a directly fused N-terminal deca-histidine tag. The expression was conducted in *E. coli* BL21(DE3) (NEB) upon the utilization of autoinduction media.[70] Therefore, chemically competent bacteria were transformed with the respective plasmids by the heat shock method, and single colonies were plated for selective growth on LB agar (lysogeny broth, Luria/Miller, Roth) containing ampicillin (amp, 100 μg/mL) at 37 °C for 17 h. A single colony was utilized for expression and used for the inoculation of a preculture of 5 mL of LB containing ampicillin (100 μg/mL). The precultures were cultivated at 37 °C, 220 rpm under darkened conditions, and the OD_{600} was monitored. Upon reaching OD_{600} of ∼0.6, 1.25 mL of precultures was used for inoculation of 50 mL of LB media supplemented with ampicillin (100 μg/mL) and containing 0.05% (w/v) glucose as well as 0.2% (w/v) lactose, and put for cultivation at 21 °C, 220 rpm for 48 h. After expression, cells were harvested by centrifugation at 4000*g*, 4 °C for 40 min. The supernatant was discarded, and the cell pellets were resuspended with 25 mL of ice-cold 20 mM MOPS pH 7.0 and stored on ice in darkened conditions. An additional centrifugation step at 4000*g*, 4 °C for 20 min allowed the removal of excess supernatant solution, thereby removing putative remaining media compounds. The pellets were again resuspended in 15 mL of 20 mM MOPS pH 7.0 and flash-frozen in liquid nitrogen prior to storage at −80 °C.

For purification of the expressed biosensors, the cells were thawed on ice in darkened conditions, and 5 mL of the cell suspension was used for cell lysis. Therefore, the cells were pelleted by centrifugation at 11000*g*, 4 °C for 1 min and suspended in 2 mL of 20 mM MOPS pH 7.0. The cell lysis was conducted by sonification for 2 rounds (Qsonica sonicators) using an amplitude of 50 and 45 pulse cycles with 3 s pulse-ON and 8 s pulse-OFF. After sonication, the cell lysates were clarified by centrifugation for 20 min at 20830*g*, 4 °C to remove cell debris. The clarified lysate containing the histidine-tagged biosensors was applied to NiNTA-based affinity chromatography (Protino, Macherey-Nagel). Therefore, 750 μL NiNTA beads were applied to a gravity flow column (Poly-Prep, Bio-Rad) and rinsed with a total volume of 30 mL deionized water. Subsequently, the beads were equilibrated with 5 mL of 20 mM MOPS at pH 7.0 prior to the application of the clarified lysate for immobilization of the histidine-tagged biosensors by gravity flow. The loaded NiNTA beads were washed with 8 mL of 20 mM MOPS at pH 7.0, 500 mM KCl, and 20 mM imidazole to remove weakly bound impurities. To elute the immobilized biosensors from the NiNTA beads, 3 mL of 20 mM MOPS at pH 7.0 and 300 mM imidazole were applied, and elution was collected in two 1.5 mL fractions. The buffer of eluted protein was exchanged upon utilization of desalting columns (Cytiva) or size exclusion chromatography via gel filtration on a Superdex 200 Increase 10/300 GL column (Cytiva), suiting further structural and biochemical characterization of the biosensor. The protein concentration was determined by UV/vis spectrometry (NanoDrop, Thermo Fisher Scientific). The purity of the elution fractions was analyzed by SDS-PAGE by conventional Coomassie staining and prior in-gel fluorescence (λ_{ex} 460 nm and λ_{em} 525 nm, Amersham ImageQuant 800, GE/Cytiva). The samples were stored for maturation at 4 °C for at least 24 h, prior to further usage for biochemical, biophysical, or structural analysis.

Functional Characterization

The screenings for optimal biochemical conditions of the Matryoshka biosensors for iron were inspired by previous studies.[70] Here, MOPS-based buffer systems were utilized.[70] Fluorescence emission spectra of the biosensors were analyzed on multimode microplate reader (Infinite M Plex, Tecan) inspired by previous protocols.[9,10,70] Therefore, the purified biosensors were diluted to 0.05−0.2 mg/mL in 20 mM MOPS pH 7.0. To assess the binding response of the biosensors to various divalent cations, titrations were conducted in microtiter plates (96 WP, flat-bottom, Greiner). Therefore, 50 mM stock solutions of the corresponding ions were generated in deionized water and utilized for subsequent stepwise dilutions to reach 50 μM stocks in 20 mM MOPS at pH 7.0. Therefore, 200 μL of the 50 μM stock solution was added to the well of lane 12 of each row (A-H) of the microtiter plate, and in all other wells, 100 μL of 20 mM MOPS pH 7.0 was added. A serial dilution was performed, reaching from 50 to 0.04 μM (from wells 12 to 2) using a multichannel pipet. Lane 1 contained only 100 μL of 20 mM MOPS at pH 7.0 and equals the 0 control. Afterward, 100 μL of the corresponding biosensor solution was added to each row of the 96 WP using a multichannel pipet. An incubation for 15 min at ambient temperature under darkened conditions ensured the binding of the ions to the biosensor. The steady-state fluorescence spectra were recorded at 25 °C in top reading mode with a bandwidth of 20 nm, 30 flashes, and manual gain of 100 for both excitation and emission wavelengths. The excitation wavelength (λ_{ex}) was 453 nm, and the emission spectra were recorded from 490 to 700 nm in 5 nm steps. The autofluorescence of the buffer was negligibly low. The reporter FP (cpsfGFP) indicated an emission maximum at 505−510 nm, and the reference FP at 600 nm. For the data evaluation, the maximal value of the reference FP at 600 nm was used for normalization of each measured data point within the recorded spectra. Furthermore, values of emission maxima were used for calculating relative dynamic range changes ($\Delta R/R_0$) in response to analyte binding by the respective biosensor as suggested previously.[9,10]

To analyze *in vivo* if in *Pseudomonas putida* the loss of siderophore production results in a detectable change of the intracellular pool of free iron ions in pyoverdine biosynthesis deletion background IronSenseR was integrated into the genome of both the *P. putida* WT strain KT2440 and the Δ*pvdD*, as described previously.[67] The resulting strains, including the WT and Δ*pvdD* strains without integration, were precultivated in 1 mL of LB at 30 °C at 1200 rpm in Flowerplates for 24 h. For biosensor-based analysis of intracellular iron levels, the cells were subsequently inoculated in 1 mL of LB with an OD_{600} of 0.05. To decrease or increase the iron availability, DIP (0.5 and 7.5 mM) and $FeSO_4$ (3.6, 10, and 50 μM) were added to the LB medium, respectively. Cells were cultivated for 4 h at 30 °C (1200 rpm). To induce the expression of the IronSenseR gene, 1 mM IPTG was added, and cells were further incubated for 48 h at 20 °C (1200 rpm). Data were obtained by three biological replicates (n = 3).

Electrocompetent *Corynebacterium glutamicum* ATCC13032 WT or Δ*dtxR* cells were transformed with the isolated pPREx2-MDtxR$_{G149}$GA plasmid via electroporation.[71] Single colonies (n = 4) were cultivated in 5 mL of BHI in reaction tubes at 30 °C for 5 h. From this preculture, a main culture with a starting OD_{600} of 0.01 was inoculated in 15 mL CGXII media containing 2% (w/v) glucose and respective amount of $FeSO_4$ as iron source (1 g L^{-1} K_2HPO_4, 1 g L^{-1} KH_2PO_4, 5 g L^{-1} urea, 42 g L^{-1} MOPS, 13.25 mg L^{-1} $CaCl_2 \cdot 2\ H_2O$,

https://doi.org/10.1021/acssensors.5c02481
ACS Sens. 2026, 11, 119−135

0.25 g L^{-1} $MgSO_4 \cdot 7\ H_2O$, 0.27/1/10 mg L^{-1} $FeSO_4 \cdot 7\ H_2O$, 10 mg L^{-1} $MnSO_4 \cdot H_2O$, 0.02 mg L^{-1} $NiCl_2 \cdot 6\ H_2O$, 0.313 mg L^{-1} $CuSO_4 \cdot 5\ H_2O$, 1 mg L^{-1} $ZnSO_4 \cdot 7\ H_2O$, 0.2 mg L^{-1} biotin, 30 mg L^{-1} 3,4-dihydroxybenzoate (PCA), 20 g L^{-1} D-glucose, pH 7.0)[72] supplemented with kanamycin (25 μg mL^{-1}), and 15 μM IPTG in 100 mL shaking flasks on a rotary shaker at 21 °C for 48 h. Consequently, cells according to an OD_{600} of 0.5 in 1 mL were harvested via centrifugation (5,000 rpm, 4 °C, 5 min) and washed twice with PBS (phosphate-buffered saline, 137 mM NaCl, 2.7 mM KCl, 10 mM Na_2HPO_4, 1.8 mM KH_2PO_4).

To ensure full maturation of the reference fluorescence protein LSSmApple, *C. glutamicum* and *P. putida* samples were stored overnight in the dark at 4 °C as described previously.[70] A volume of 100 μL was analyzed using a multimode microplate reader (Infinite M1000Pro, Tecan) by recording emission spectra from 490 nm to 700 nm in 5 nm increments, with single-wavelength excitation at 453 nm and using the maximal value of the reference FP at 600 nm for normalization as described above in the methods section.

Analysis of Biosensor Kinetics

To determine the sensing mode of the proposed biosensors and to obtain comparable data, the dynamic range $[\Delta R/R_0]$,[10] dynamic range in percent $[\Delta R/R_0, \%]$, and the signal to reference correlation $[\Delta R/F_R]$ were calculated by the following equations

$$R - R_0 = \Delta R \qquad \frac{R - R_0}{R_0} = [\Delta R/R_0]$$

$$\Delta R/R_0 \times 100 = [\Delta R/R_0]\ \text{in}\ \%$$

$$\frac{F_{GFP_{max}} - F_{GFP_{min}}}{F_{LSSmApple}} = [\Delta R/F_R]$$

R_0: Fluorescence emmsion intensety ratio (cpsfGFP/LSSmApple) prior addition of ligand.

R: Fluorescence emmsion intensety ratio (cpsfGFP/LSSmApple) upon increasing ligand concentration.

$F_{GFP_{max}}$: Fluorescence emission of cpsfGFP at 510 nm at the highest metabolite concentration.

$F_{GFP_{min}}$: Fluorescence emission of cpsfGFP at 510 nm without metabolite.

$F_{LSSmApple}$: Highest emission of the reference FP at 600 nm throughout the assay.

The binding affinity was determined by fitting the obtained titration data. The reported K_d values are calculated by the concentration-dependent X values whereby four-parameter logistic (4PL, X is concentration and not log concentration X) was used in a dose−response model to determine the IC50 of the agonist (ferrous iron), which is the concentration that causes a response halfway between the "bottom" (basal) and "top" (maximal) response.

$$\frac{X^{\text{HillSlope}}(\text{Top} - \text{Bottom})}{X^{\text{HillSlope}} + \text{IC}_{50}^{\text{HillSlope}}} + \text{Bottom} = Y$$

Detailed instructions, including the interpret parameters (IC50, Hill Slope, Top and Bottom plateaus of the Y axis) given by GraphPad Prism 10.4.0 (527) (GraphPad Software, LLC). The representative IC50 is equal to the K_d values. The error is indicated as the standard error of the mean (SEM) obtained by at least three biological replicates (n = 3).

Fluorescence Microscopy

Escherichia coli BL21(DE3) were transformed with a plasmid encoding for IronSenseR ($MDtxR_{G149}GA$, WT) or binding-deficient mutants of IronSenseR (H79A, H98A, and C102A) and cultivated as described above for 24 h in a volume of 20 mL. Prior to imaging, cells were washed with PBS buffer (Phosphate Buffered Saline, 137 mM NaCl, 2.7 mM KCl, 10 mM Na_2HPO_4, 1.8 mM KH_2PO_4) and incubated for 20 min with PBS buffer containing 0 μM, 20 μM, or 250 μM 2,2′-bipyridine (BPD). Cells were immobilized on poly-L-lysine-coated 8 Well μ-Slides (ibidi). Imaging was performed using an Olympus Fluoview 3000 confocal laser scanning microscope equipped with a 60× UPLSAPO water objective (NA 1.2). Samples containing IronSenseR were excited with a 488 nm laser (0.5% laser power). Pixel dwell time was set to 2 μs with a line averaging of 2 and a pinhole diameter of 1 AU. Detector range was set to 500−530 nm for cpsfGFP. Fluorescence of LSSmApple was collected at 600−700 nm. Six biological replicates (n = 6) for the WT and three biological replicates (n = 3) for the binding-deficient mutants were analyzed.

Image Processing and Image Data Analysis

For the ratiometric intensity analysis, a segmentation was performed using Cellpose 2.0 (Version 2.2)[73] with the pretrained "cyto2" model and quantified as well as plotted using a custom python script. Total intensity for the green channel (cpsfGFP, 500−530 nm) and red channel (LSSmApple, 600−700 nm) was extracted from the resulting masks and used to calculate the respective ratios. Low and nonexpressing cells with an excessively low intensity in either channel were excluded from the analysis using an intensity threshold of 200. This threshold separated best the two peaks (expressing VS nonexpressing) of the distribution of individual bacteria mean fluorescence intensities. Fluorescence ratios for all conditions of each biological replicate were normalized to the PBS measurements of the respective replicate. The fluorescence ratios were plotted using a boxplot and a strip plot. For visualization of fluorescence ratios, exemplary images were processed in FIJI.[74] The transmitted light channel was thresholded using either the "Otsu" or "Triangle" method followed by a "Dilate" and an "Open" step. The resulting mask was used for segmentation of fluorescence channels, while objects smaller than 0.3 μm^2 were excluded. A fluorescence ratio channel was created by dividing the pixel intensities of the green channel by the pixel intensities of the red channel. The resulting image was smoothed using a median filter with a radius of 2. After that, the normalization factor calculated before was applied to the ratio image. Resulting ratios were displayed using a rainbow-colored lookup table ("physics" in FIJI) ranging from 0.6 to 1.1.

Structural Modeling

The structural models were created upon utilization of AlphaFold3 prediction algorithm.[35,36] The default criteria given by AlphaFold algorithm were used.[35,36] Five models were generated by entering the amino acid sequence of the proposed biosensors to the AlphaFold server.[36] Model ranking numbers were from 0 to 4 and were sorted by ranking score. Model 0 represents the model with the highest ranking score among the predicted structural models for each biosensor. If models possess the same ranking score, still model 0 was used. Additionally, the predicted local Distance Distribution Test (pIDDT) was utilized to view on the predicted modeling data.[75] Only highly confident models were generated and used, based on plDDT view.[75] The corresponding data can be found in the Supporting Information (Figure S7). For the retrospective analysis of CoBiSe, the AF3 models available at UniProtKB were utilized.

Structural Analysis by Small-Angle X-ray Scattering

SEC-SAXS data was acquired on beamline BM29 at the ESRF Grenoble.[76] The BM29 beamline was equipped with a PILATUS 2 M detector (Dectris) at a fixed distance of 2.827 m.

IronSenseR was purified as described beforehand and utilized for structural analysis by SEC-SAXS with a concentration of 4 mg/mL in 20 mM MOPS pH 7.0, 250 mM KCl, and an injection volume of 100 μL. The SEC-SAXS runs were performed at 20 °C on a Superdex 200 increase 10/300 GL column with a flow rate of 0.6 mL/min. We collected 1200 frames with an exposure time of 2 s/frame. Data were scaled to the absolute intensity against water. All used programs for data processing were part of the ATSAS Software package (Version 3.0.5).[77] Primary data reduction was performed with the programs CHROMIXS[78] and PRIMUS.[79] With the Guinier approximation,[80] we determine the forward scattering $I(0)$ and the radius of gyration (R_g). The program GNOM[81] was used to estimate the maximum particle dimension (D_{max}) with the pair-distribution function $p(r)$. We created a model of $MDtxR_{G149}GA$ with AlphaFold3[35,36] and

https://doi.org/10.1021/acssensors.5c02481
ACS Sens. 2026, 11, 119−135

compared the theoretical scattering intensity of the resulting models against the experimental data with CRYSOL.[82]

■ ASSOCIATED CONTENT

Data Availability Statement

The data of the present study are included in the published article and the Supporting Information. Further data, including the corresponding raw data, is deposited in the Data Hub[83] (URL: https://git.nfdi4plants.org). The FAIR data publication can be found under DOI: 10.60534/8s9sz-psy95. The imaging data is deposited at Bioimage archive[84] accession number S-BIAD2396 (DOI: 10.6019/S-BIAD2396). The structural data is deposited at SASBDB[85] (Accession code SASDWP9).

Supporting Information

The Supporting Information is available free of charge at https://pubs.acs.org/doi/10.1021/acssensors.5c02481.

Additional experimental details and data, including the detailed evaluation of the retrospective CoBiSe for pre-existing biosensors and DtxR, the SDS-PAGE analysis of purified biosensors, fluorescence spectra of *in vitro* ion titrations, *in vivo* imaging and evaluation, *in vivo* analysis of *C. glutamicum* and *P. putida*, scattering data of SAXS, scoring data and confidence of biosensor models, overall SAXS data, list of primers, microbiological information (strains and plasmids), supplemental sequences, and references (PDF)

■ AUTHOR INFORMATION

Corresponding Authors

Sander H. J. Smits − *Center for Structural Studies, Faculty of Mathematics and Natural Sciences and Institute for Biochemistry, Faculty of Mathematics and Natural Sciences, Heinrich Heine University Düsseldorf, 40225 Düsseldorf, Germany;* orcid.org/0000-0003-0780-9251; Email: sander.smits@hhu.de

Christoph G. W. Gertzen − *Center for Structural Studies, Faculty of Mathematics and Natural Sciences and Institute for Pharmaceutical and Medicinal Chemistry, Faculty of Mathematics and Natural Sciences, Heinrich Heine University Düsseldorf, 40225 Düsseldorf, Germany;* Email: christoph.gertzen@hhu.de

Authors

Athanasios Papadopoulos − *Center for Structural Studies, Faculty of Mathematics and Natural Sciences, Heinrich Heine University Düsseldorf, 40225 Düsseldorf, Germany*

Manuel T. Anlauf − *Center for Advanced Imaging, Faculty of Mathematics and Natural Sciences, Heinrich Heine University Düsseldorf, 40225 Düsseldorf, Germany*

Jens Reiners − *Center for Structural Studies, Faculty of Mathematics and Natural Sciences, Heinrich Heine University Düsseldorf, 40225 Düsseldorf, Germany*

Seung-Hyun Paik − *Institute of Molecular Enzyme Technology, Faculty of Mathematics and Natural Sciences, Heinrich Heine University Düsseldorf, 52428 Jülich, Germany*

Aileen Krüger − *Institute of Microbial Interactions, Faculty of Mathematics and Natural Sciences, Heinrich Heine University Düsseldorf, 40225 Düsseldorf, Germany*

Benita Lückel − *Institute of Microbial Interactions, Faculty of Mathematics and Natural Sciences, Heinrich Heine University Düsseldorf, 40225 Düsseldorf, Germany*

Michael Bott − *Institute of Microbial Interactions, Faculty of Mathematics and Natural Sciences, Heinrich Heine University Düsseldorf, 40225 Düsseldorf, Germany*

Thomas Drepper − *Institute of Molecular Enzyme Technology, Faculty of Mathematics and Natural Sciences, Heinrich Heine University Düsseldorf, 52428 Jülich, Germany*

Julia Frunzke − *Institute of Microbial Interactions, Faculty of Mathematics and Natural Sciences, Heinrich Heine University Düsseldorf, 40225 Düsseldorf, Germany; Institute of Bio- and Geosciences (IBG-1: Biotechnology), 52428 Jülich, Germany;* orcid.org/0000-0001-6209-7950

Holger Gohlke − *Institute of Bio- and Geosciences (IBG-4: Bioinformatics), 52428 Jülich, Germany; Institute for Pharmaceutical and Medicinal Chemistry, Faculty of Mathematics and Natural Sciences, Heinrich Heine University Düsseldorf, 40225 Düsseldorf, Germany*

Stefanie Weidtkamp-Peters − *Center for Advanced Imaging, Faculty of Mathematics and Natural Sciences, Heinrich Heine University Düsseldorf, 40225 Düsseldorf, Germany*

Complete contact information is available at: https://pubs.acs.org/10.1021/acssensors.5c02481

Author Contributions

A.P., C.G., and S.S. initiated this study. A.P. conducted the biosensor design, molecular bioengineering, and protein characterization. C.G., A.P., J.R., and H.G. conducted the computational analysis (CNA and structure prediction). A.P. and C.G. initiated the idea of CoBiSe. M.A., T.B., and S.W.P. conducted the microscopy and imaging evaluation. S.P. and T.D. conducted *in vivo* experiments in *P. putida*. A.K., B.L., and J.F. conducted *in vivo* experiments in *C. glutamicum*. A.P., C.G., and S.S. supervised the study. S.S. coordinated funding and project administration. A.P. and S.S. wrote the initial manuscript. All authors contributed to fruitful discussions and lively development of the manuscript. Correspondence and requests for materials should be addressed to Athanasios Papadopoulos, Sander Smits, or Christoph G.W. Gertzen.

Funding

The research was supported by the German Research Foundation (DFG) through the Collaborative Research Center 1535 Microbial Networking (MibiNet, CRC/SFB 1535) Project ID 45809666 (Z01 to S.W.P. and S.S., B01 to J.F. and T.D.). The Center for Structural Studies (CSS) is funded by DFG, projects 417919780 and INST 208/761−1 FUGG. Center of Advanced Imaging is funded by DFG, project 284074525 and project I3D:bio, DFG Grant Number: 462231789.

Notes

The authors declare no competing financial interest.

■ ACKNOWLEDGMENTS

We would like to thank Wolf B. Frommer for inspiring and very valuable discussions and for sharing with us research objectives on Matryoshka biosensor design. Our special thanks to the Institute for Biochemistry for their friendly support in laboratory equipment. We acknowledge the European Synchrotron Radiation Facility (ESRF) for the provision of

synchrotron radiation facilities, and we would like to thank Dihia Moussaoui, Mark Tully, and Anton Popov for assistance in using beamline BM29. We also acknowledge DESY (Hamburg, Germany), a member of the Helmholtz Association HGF, for the provision of experimental facilities. Parts of this research were carried out at PETRA III, and we would like to thank Cy M. Jeffries and Dmytro Soloviov (EMBL Hamburg) for assistance in using beamline P12. Computational support and infrastructure were provided by the "Zentrum für Informations- und Medientechnologie" (ZIM) at Heinrich Heine University Düsseldorf.

■ ABBREVIATIONS

MRE, Molecular recognition element; FP, fluorescent protein; FRET, Förster resonance energy transfer; cpFP, circular-permutated fluorophore; sfGFP, superfolder green fluorescent protein; LSS, large Stokes shift; Single-FP, single-fluorescent protein or fluorophore; CNA, constraint network analysis; ENT^{FNC}, ensembles of network topologies and fuzzy non-covalent constraints; DtxR, diphtheria toxin regulator protein; BPD, 2,2′-Bipyridine; ROS, reactive oxygen species

■ REFERENCES

(1) Frei, M. S.; Mehta, S.; Zhang, J. Next-Generation Genetically Encoded Fluorescent Biosensors Illuminate Cell Signaling and Metabolism. *Annu. Rev. Biophys.* **2024**, *53*, 275−297.
(2) Kim, H.; Ju, J.; Lee, H. N.; Chun, H.; Seong, J. Genetically Encoded Biosensors Based on Fluorescent Proteins. *Sensors* **2021**, *21*, No. 795.
(3) Wang, M.; Da, Y.; Tian, Y. Fluorescent proteins and genetically encoded biosensors. *Chem. Soc. Rev.* **2023**, *52*, 1189−1214.
(4) Greenwald, E. C.; Mehta, S.; Zhang, J. Genetically Encoded Fluorescent Biosensors Illuminate the Spatiotemporal Regulation of Signaling Networks. *Chem. Rev.* **2018**, *118*, 11707−11794.
(5) Nadler, D. C.; Morgan, S. A.; Flamholz, A.; Kortright, K. E.; Savage, D. F. Rapid construction of metabolite biosensors using domain-insertion profiling. *Nat. Commun.* **2016**, *7*, No. 12266.
(6) Sadoine, M.; Ishikawa, Y.; Kleist, T. J.; Wudick, M. M.; Nakamura, M.; Grossmann, G.; Frommer, W. B.; Ho, C. H. Designs, applications, and limitations of genetically encoded fluorescent sensors to explore plant biology. *Plant Physiol.* **2021**, *187*, 485−503.
(7) Nasu, Y.; Shen, Y.; Kramer, L.; Campbell, R. E. Structure- and mechanism-guided design of single fluorescent protein-based biosensors. *Nat. Chem. Biol.* **2021**, *17*, 509−518.
(8) Akerboom, J.; Rivera, J. D.; Guilbe, M. M.; et al. Crystal structures of the GCaMP calcium sensor reveal the mechanism of fluorescence signal change and aid rational design. *J. Biol. Chem.* **2009**, *284*, 6455−6464.
(9) Ast, C.; Foret, J.; Oltrogge, L. M.; De Michele, R.; Kleist, T. J.; Ho, C. H.; Frommer, W. B. Ratiometric Matryoshka biosensors from a nested cassette of green- and orange-emitting fluorescent proteins. *Nat. Commun.* **2017**, *8*, No. 431.
(10) Ejike, J. O.; Sadoine, M.; Shen, Y.; et al. A Monochromatically Excitable Green-Red Dual-Fluorophore Fusion Incorporating a New Large Stokes Shift Fluorescent Protein. *Biochemistry* **2024**, *63*, 171−180.
(11) Tainaka, K.; Sakaguchi, R.; Hayashi, H.; Nakano, S.; Liew, F. F.; Morii, T. Design strategies of fluorescent biosensors based on biological macromolecular receptors. *Sensors* **2010**, *10*, 1355−1376.
(12) Koveal, D.; Rosen, P. C.; Meyer, D. J.; Diaz-Garcia, C. M.; Wang, Y.; Cai, L. H.; Chou, P. J.; Weitz, D. A.; Yellen, G. A high-throughput multiparameter screen for accelerated development and optimization of soluble genetically encoded fluorescent biosensors. *Nat. Commun.* **2022**, *13*, No. 2919.
(13) Kaczmarski, J. A.; Mitchell, J. A.; Spence, M. A.; Vongsouthi, V.; Jackson, C. J. Structural and evolutionary approaches to the design and optimization of fluorescence-based small molecule biosensors. *Curr. Opin. Struct. Biol.* **2019**, *57*, 31−38.
(14) Ostermeier, M. Engineering allosteric protein switches by domain insertion. *Protein Eng., Des. Sel.* **2005**, *18*, 359−364.
(15) Berrondo, M.; Ostermeier, M.; Gray, J. J. Structure prediction of domain insertion proteins from structures of individual domains. *Structure* **2008**, *16*, 513−527.
(16) Collinet, B.; Hervé, M.; Pecorari, F.; Minard, P.; Eder, O.; Desmadril, M. Functionally accepted insertions of proteins within protein domains. *J. Biol. Chem.* **2000**, *275*, 17428−17433.
(17) Betton, J.-M.; Jacob, J. P.; Hofnung, M.; Broome-Smith, J. K. Creating a bifunctional protein by insertion of *β*-lactamase into the maltodextrin-binding protein. *Nat. Biotechnol.* **1997**, *15*, 1276−1279.
(18) Edwards, W. R.; Busse, K.; Allemann, R. K.; Jones, D. D. Linking the functions of unrelated proteins using a novel directed evolution domain insertion method. *Nucleic Acids Res.* **2008**, *36*, No. e78.
(19) Bilan, D. S.; Pase, L.; Joosen, L.; et al. HyPer-3: a genetically encoded H(2)O(2) probe with improved performance for ratiometric and fluorescence lifetime imaging. *ACS Chem. Biol.* **2013**, *8*, 535−542.
(20) Yaginuma, H.; Kawai, S.; Tabata, K. V.; Tomiyama, K.; Kakizuka, A.; Komatsuzaki, T.; Noji, H.; Imamura, H. Diversity in ATP concentrations in a single bacterial cell population revealed by quantitative single-cell imaging. *Sci. Rep.* **2014**, *4*, No. 6522.
(21) Bilan, D. S.; Matlashov, M. E.; Gorokhovatsky, A. Y.; Schultz, C.; Enikolopov, G.; Belousov, V. V. Genetically encoded fluorescent indicator for imaging NAD(+)/NADH ratio changes in different cellular compartments. *Biochim. Biophys. Acta* **2014**, *1840*, 951−957.
(22) Tantama, M.; Martinez-Francois, J. R.; Mongeon, R.; Yellen, G. Imaging energy status in live cells with a fluorescent biosensor of the intracellular ATP-to-ADP ratio. *Nat. Commun.* **2013**, *4*, No. 2550.
(23) Brune, I.; Werner, H.; Hüser, A. T.; Kalinowski, J.; Pühler, A.; Tauch, A. The DtxR protein acting as dual transcriptional regulator directs a global regulatory network involved in iron metabolism of *Corynebacterium glutamicum*. *BMC Genomics* **2006**, *7*, No. 21.
(24) Wennerhold, J.; Bott, M. The DtxR regulon of *Corynebacterium glutamicum*. *J. Bacteriol.* **2006**, *188*, 2907−2918.
(25) Tao, X.; Boyd, J.; Murphy, J. R. Specific binding of the diphtheria tox regulatory element DtxR to the tox operator requires divalent heavy metal ions and a 9-base-pair interrupted palindromic sequence. *Proc. Natl. Acad. Sci. U.S.A.* **1992**, *89*, 5897−5901.
(26) D'Aquino, J. A.; Tetenbaum-Novatt, J.; White, A.; Berkovitch, F.; Ringe, D. Mechanism of metal ion activation of the diphtheria toxin repressor DtxR. *Proc. Natl. Acad. Sci. U.S.A.* **2005**, *102*, 18408−18413.
(27) Pohl, E.; Goranson-Siekierke, J.; Choi, M. K.; Roosild, T.; Holmes, R. K.; Hol, W. G. Structures of three diphtheria toxin repressor (DtxR) variants with decreased repressor activity. *Acta Crystallogr. D: Biol. Crystallogr.* **2001**, *57*, 619−627.
(28) Ding, X.; Zeng, H.; Schiering, N.; Ringe, D.; Murphy, J. R. Identification of the primary metal ion-activation sites of the diphtheria tox represser by X-ray crystallography and site-directed mutational analysis. *Nat. Struct. Mol. Biol.* **1996**, *3*, 382−387.
(29) Soleja, N.; Mohsin, M. A genetically encoded probe for monitoring and detection of iron in real-time. *Sens. Diagn.* **2024**, *3*, 1714−1723.
(30) Sevimli, G.; Alston, A. E.; Funk, F.; Fluhmann, B.; Malli, R.; Graier, W. F.; Eroglu, E. Probing Subcellular Iron Availability with Genetically Encoded Nitric Oxide Biosensors. *Biosensors* **2022**, *12*, No. 903.
(31) Sangokoya, C. The genetically encoded biosensor FEOX is a molecular gauge for cellular iron environment dynamics at single cell resolution. *Sci. Rep.* **2025**, *15*, No. 36596.
(32) Sangokoya, C. The FIRE biosensor illuminates iron regulatory protein activity and cellular iron homeostasis. *Cell Rep. Methods* **2025**, *5*, No. 100960.
(33) Akyol, A.; Çimen, Ş.; Gottschalk, B.; et al. Tracking Intracellular Labile Iron with a Genetically Encoded Fluorescent

Reporter System Based on Protein Stability. *ACS Sens.* **2025**, *10*, 5854−5861.
(34) Torres-Ocampo, A. P.; Palmer, A. E. Genetically encoded fluorescent sensors for metals in biology. *Curr. Opin. Chem. Biol.* **2023**, *74*, No. 102284.
(35) Jumper, J.; Evans, R.; Pritzel, A.; et al. Highly accurate protein structure prediction with AlphaFold. *Nature* **2021**, *596*, 583−589.
(36) Abramson, J.; Adler, J.; Dunger, J.; et al. Accurate structure prediction of biomolecular interactions with AlphaFold 3. *Nature* **2024**, *630*, 493−500.
(37) Pfleger, C.; Rathi, P. C.; Klein, D. L.; Radestock, S.; Gohlke, H. Constraint Network Analysis (CNA): a Python software package for efficiently linking biomacromolecular structure, flexibility, (thermo-)stability, and function. *J. Chem. Inf Model* **2013**, *53*, 1007−1015.
(38) Pfleger, C.; Gohlke, H. Efficient and robust analysis of biomacromolecular flexibility using ensembles of network topologies based on fuzzy noncovalent constraints. *Structure* **2013**, *21*, 1725−1734.
(39) Belousov, V. V.; Fradkov, A. F.; Lukyanov, K. A.; Staroverov, D. B.; Shakhbazov, K. S.; Terskikh, A. V.; Lukyanov, S. Genetically encoded fluorescent indicator for intracellular hydrogen peroxide. *Nat. Methods* **2006**, *3*, 281−286.
(40) Li, S.; Crooks, P. A.; Wei, X.; de Leon, J. Toxicity of dipyridyl compounds and related compounds. *Crit. Rev. Toxicol.* **2004**, *34*, 447−460.
(41) Hoyer, J.; Bartel, J.; Gómez-Mejia, A.; et al. Proteomic response of Streptococcus pneumoniae to iron limitation. *Int. J. Med. Microbiol.* **2018**, *308*, 713−721.
(42) Andrews, S. C.; Robinson, A. K.; Rodriguez-Quinones, F. Bacterial iron homeostasis. *FEMS Microbiol. Rev.* **2003**, *27*, 215−237.
(43) Martínez-García, E.; de Lorenzo, V. *Pseudomonas putida* as a synthetic biology chassis and a metabolic engineering platform. *Curr. Opin. Biotechnol.* **2024**, *85*, No. 103025.
(44) Becker, F.; Wienand, K.; Lechner, M.; Frey, E.; Jung, H. Interactions mediated by a public good transiently increase cooperativity in growing *Pseudomonas putida* metapopulations. *Sci. Rep.* **2018**, *8*, No. 4093.
(45) Ringel, M. T.; Bruser, T. The biosynthesis of pyoverdines. *Microb. Cell* **2018**, *5*, 424−437.
(46) Merkx, M.; Smith, B.; Jewett, M. Engineering Sensor Proteins. *ACS Sens.* **2019**, *4*, 3089−3091.
(47) Hensen, U.; Meyer, T.; Haas, J.; Rex, R.; Vriend, G.; Grubmüller, H. Exploring protein dynamics space: the dynasome as the missing link between protein structure and function. *PLoS One* **2012**, *7*, No. e33931.
(48) Frawley, E. R.; Fang, F. C. The ins and outs of bacterial iron metabolism. *Mol. Microbiol.* **2014**, *93*, 609−616.
(49) Ratledge, C.; Dover, L. G. Iron metabolism in pathogenic bacteria. *Annu. Rev. Microbiol.* **2000**, *54*, 881−941.
(50) Bradley, J. M.; Svistunenko, D. A.; Wilson, M. T.; Hemmings, A. M.; Moore, G. R.; Le Brun, N. E. Bacterial iron detoxification at the molecular level. *J. Biol. Chem.* **2020**, *295*, 17602−17623.
(51) Choe, M.; Titov, D. V. Genetically encoded tools for measuring and manipulating metabolism. *Nat. Chem. Biol.* **2022**, *18*, 451−460.
(52) Ewald, J. C.; Reich, S.; Baumann, S.; Frommer, W. B.; Zamboni, N. Engineering genetically encoded nanosensors for real-time in vivo measurements of citrate concentrations. *PLoS One* **2011**, *6*, No. e28245.
(53) Koveal, D.; Diaz-Garcia, C. M.; Yellen, G. Fluorescent Biosensors for Neuronal Metabolism and the Challenges of Quantitation. *Curr. Opin. Neurobiol.* **2020**, *63*, 111−121.
(54) Rathi, P. C.; Mulnaes, D.; Gohlke, H. VisualCNA: a GUI for interactive constraint network analysis and protein engineering for improving thermostability. *Bioinformatics* **2015**, *31*, 2394−2396.
(55) UniProt, C. UniProt: a worldwide hub of protein knowledge. *Nucleic Acids Res.* **2019**, *47*, D506−D515.
(56) Nakamura, A.; Sosa, A.; Komori, H.; Kita, A.; Miki, K. Crystal structure of TTHA1657 (AT-rich DNA-binding protein; p25) from Thermus thermophilus HB8 at 2.16 A resolution. *Proteins* **2007**, *66*, 755−759.
(57) Yagi, H.; Kajiwara, N.; Tanaka, H.; Tsukihara, T.; Kato-Yamada, Y.; Yoshida, M.; Akutsu, H. Structures of the thermophilic F1-ATPase epsilon subunit suggesting ATP-regulated arm motion of its C-terminal domain in F1. *Proc. Natl. Acad. Sci. U.S.A.* **2007**, *104*, 11233−11238.
(58) Diez, J.; Diederichs, K.; Greller, G.; Horlacher, R.; Boos, W.; Welte, W. The crystal structure of a liganded trehalose/maltose-binding protein from the hyperthermophilic Archaeon Thermococcus litoralis at 1.85 A. *J. Mol. Biol.* **2001**, *305*, 905−915.
(59) Rostkowski, M.; Olsson, M. H.; Sondergaard, C. R.; Jensen, J. H. Graphical analysis of pH-dependent properties of proteins predicted using PROPKA. *BMC Struct. Biol.* **2011**, *11*, No. 6.
(60) Hensen, U.; Meyer, T.; Haas, J.; Rex, R.; Vriend, G.; Grubmuller, H. Exploring protein dynamics space: the dynasome as the missing link between protein structure and function. *PLoS One* **2012**, *7*, No. e33931.
(61) Schrödinger, L. L. C. *Edn. Version 2.5*, 2022.
(62) Pédelacq, J.-D.; Cabantous, S.; Tran, T.; Terwilliger, T. C.; Waldo, G. S. Engineering and characterization of a superfolder green fluorescent protein. *Nat. Biotechnol.* **2006**, *24*, 79−88.
(63) Claassens, N. J.; Siliakus, M. F.; Spaans, S. K.; Creutzburg, S. C. A.; Nijsse, B.; Schaap, P. J.; Quax, T. E. F.; van der Oost, J. Improving heterologous membrane protein production in *Escherichia coli* by combining transcriptional tuning and codon usage algorithms. *PLoS One* **2017**, *12*, No. e0184355.
(64) Gibson, D. G.; Young, L.; Chuang, R. Y.; Venter, J. C.; Hutchison, C. A., III; Smith, H. O. Enzymatic assembly of DNA molecules up to several hundred kilobases. *Nat. Methods* **2009**, *6*, 343−345.
(65) Choi, K. H.; Schweizer, H. P. mini-Tn7 insertion in bacteria with single attTn7 sites: example Pseudomonas aeruginosa. *Nat. Protoc.* **2006**, *1*, 153−161.
(66) Volke, D. C.; Friis, L.; Wirth, N. T.; Turlin, J.; Nikel, P. I. Synthetic control of plasmid replication enables target- and self-curing of vectors and expedites genome engineering of *Pseudomonas putida*. *Metab. Eng. Commun.* **2020**, *10*, No. e00126.
(67) Wynands, B.; Lenzen, C.; Otto, M.; Koch, F.; Blank, L. M.; Wierckx, N. Metabolic engineering of Pseudomonas taiwanensis VLB120 with minimal genomic modifications for high-yield phenol production. *Metab. Eng.* **2018**, *47*, 121−133.
(68) Bakkes, P. J.; Ramp, P.; Bida, A.; Dohmen-Olma, D.; Bott, M.; Freudl, R. Improved pEKEx2-derived expression vectors for tightly controlled production of recombinant proteins in *Corynebacterium glutamicum*. *Plasmid* **2020**, *112*, No. 102540.
(69) Sambrook, J.; Fritsch, E.; Maniatis, T. *Molecular Cloning: a Laboratory Manual.*; Cold Spring Harbor Laboratory Press: Plainview. New York, 1989; Chapter 1, Vol. *16*, p 66.
(70) Sadoine, M.; Castro-Rodriguez, V.; Poloczek, T.; Javot, H.; Sunal, E.; Wudick, M. M.; Frommer, W. B. Affinity Purification of GO-Matryoshka Biosensors from *E. coli* for Quantitative Ratiometric Fluorescence Analyses. *Bio. Protoc.* **2020**, *10*, No. e3773.
(71) van der Rest, M. E.; Lange, C.; Molenaar, D. A heat shock following electroporation induces highly efficient transformation of *Corynebacterium glutamicum* with xenogeneic plasmid DNA. *Appl. Microbiol. Biotechnol.* **1999**, *52*, 541−545.
(72) Keilhauer, C.; Eggeling, L.; Sahm, H. Isoleucine synthesis in *Corynebacterium glutamicum*: molecular analysis of the ilvB-ilvN-ilvC operon. *J. Bacteriol.* **1993**, *175*, 5595−5603.
(73) Pachitariu, M.; Stringer, C. Cellpose 2.0: how to train your own model. *Nat. Methods* **2022**, *19*, 1634−1641.
(74) Schindelin, J.; Arganda-Carreras, I.; Frise, E.; et al. Fiji: an open-source platform for biological-image analysis. *Nat. Methods* **2012**, *9*, 676−682.
(75) Mariani, V.; Biasini, M.; Barbato, A.; Schwede, T. lDDT: a local superposition-free score for comparing protein structures and models using distance difference tests. *Bioinformatics* **2013**, *29*, 2722−2728.

https://doi.org/10.1021/acssensors.5c02481
ACS Sens. 2026, 11, 119−135

(76) Tully, M. D.; Kieffer, J.; Brennich, M. E.; et al. BioSAXS at European Synchrotron Radiation Facility - Extremely Brilliant Source: BM29 with an upgraded source, detector, robot, sample environment, data collection and analysis software. *J. Synchrotron Radiat.* **2023**, *30*, 258−266.
(77) Manalastas-Cantos, K.; Konarev, P. V.; Hajizadeh, N. R.; et al. ATSAS 3.0: expanded functionality and new tools for small-angle scattering data analysis. *J. Appl. Crystallogr.* **2021**, *54*, 343−355.
(78) Panjkovich, A.; Svergun, D. I. CHROMIXS: automatic and interactive analysis of chromatography-coupled small angle X-ray scattering data. *Bioinformatics* **2017**, *34* (11), 1944−1946, DOI: 10.1093/bioinformatics/btx846.
(79) Konarev, P. V.; Volkov, V. V.; Sokolova, A. V.; Koch, M. H. J.; Svergun, D. I. PRIMUS: a Windows PC-based system for small-angle scattering data analysis. *J. Appl. Crystallogr.* **2003**, *36*, 1277−1282.
(80) Guinier, A. Small-angle X-ray diffraction: application to the study of ultramicroscopic phenomena. *Ann. Phys.* **1939**, *11*, 161−237.
(81) Svergun, D. I. Determination of the Regularization Parameter in Indirect-Transform Methods Using Perceptual Criteria. *J. Appl. Crystallogr.* **1992**, *25*, 495−503.
(82) Svergun, D.; Barberato, C.; Koch, M. H. J. CRYSOL− a Program to Evaluate X-ray Solution Scattering of Biological Macromolecules from Atomic Coordinates. *J. Appl. Crystallogr.* **1995**, *28*, 768−773.
(83) Weil, H. L.; Schneider, K.; Tschöpe, M.; et al. PLANTdata-HUB: a collaborative platform for continuous FAIR data sharing in plant research. *Plant J.* **2023**, *116*, 974−988.
(84) Hartley, M.; Kleywegt, G. J.; Patwardhan, A.; Sarkans, U.; Swedlow, J. R.; Brazma, A. The BioImage Archive - Building a Home for Life-Sciences Microscopy Data. *J. Mol. Biol.* **2022**, *434*, No. 167505.
(85) Kikhney, A. G.; Borges, C. R.; Molodenskiy, D. S.; Jeffries, C. M.; Svergun, D. I. SASBDB: Towards an automatically curated and validated repository for biological scattering data. *Protein Sci.* **2020**, *29*, 66−75.